nature cardiovascular research



Article

https://doi.org/10.1038/s44161-025-00740-z

Single-cell profiling reveals three endothelial-to-hematopoietic transitions with divergent isoform expression landscapes

Received: 17 September 2024

Accepted: 30 September 2025

Published online: 11 November 2025

Check for updates

Wen Hao Neo^{1,14}, Muhammad Zaki Hidayatullah Fadlullah (a.2,14), Harshangda Bhatnagar^{1,3}, Cristiana Barone⁴, Giulia Quattrini⁴, Filipa Timóteo-Ferreira (a.4), Joana Carrelha^{5,6}, Gianluca Sala⁴, Robert Sellers⁷, John Weightman⁸, Wolfgang Breitwieser⁸, Natalia Moncaut⁹, Roshana Thambyrajah (a.1), Sten Eirik W. Jacobsen (a.1), Mudassar Iqbal³, Syed Murtuza Baker (a.2), Emanuele Azzoni (a.1), Michael Lie-A-Ling (a.2), Georges Lacaud (a.2)

Hemogenic endothelium (HE) is recognized as the origin of all definitive blood cells, including hematopoietic stem cells (HSCs); however, the mechanisms governing the hematopoietic progenitor versus HSC fate choice within the HE remain unknown. Here we combine differentiation assays with full-length single-cell transcriptome data for extra-embryonic yolk sac (YS) and intra-embryonic aorta-gonad-mesonephros (AGM) region HE populations. We identified and localized three differentiation trajectories, each containing a distinct HE subset: erythromyeloid progenitor-primed HE in the YS plexus, lymphomyeloid progenitor-primed HE in large YS arteries and hematopoietic stem and progenitor cell-primed HE in the AGM. Chromatin modifiers and spliceosome components were enriched in AGM HE. This correlated with a higher isoform complexity of the AGM HE transcriptome. Distinct AGM HE-specific isoform expression patterns were observed for a broad range of genes, including stemness-associated factors like *Runx1*. Our data form a unique resource for studying cell fate decisions in different HE populations.

A pivotal step during mammalian ontogeny is the establishment of the hematopoietic system, which unfolds in three successive, partially overlapping waves^{1,2}. The first two waves takes place in the yolk sac (YS). Wave 1 generates primitive erythrocytes and macrophages (E7.5)^{3,4}. Wave 2 sequentially gives rise to erythromyeloid progenitors (EMPs; E8.25)^{4,5} and lymphomyeloid progenitors (LMPs; E9.5)^{6,7}. The final wave, in the intra-embryonic aorta–gonad–mesonephros (AGM) region, produces hematopoietic stem and progenitor cells (HSPCs; wave-3, E10.5)^{8,9}. In recent years, it has become evident that wave 2 cells not only play a role in wave 3 HSC generation but can also persist

into adulthood \$^{2,10,11}\$. The hematopoietic cells in wave 2 and wave 3, also known as the definitive waves, arise from a specific endothelium, called hemogenic endothelium (HE), through a process called endothelial-to-hematopoietic transition (EHT) $^{12-16}$ orchestrated by the transcription factors RUNX1 (refs. 13,17–19) and GFI1 (refs. 20,21).

A critical question in hematopoietic development is why the HE in the extra-embryonic space is skewed toward EMP and LMP generation, whereas intra-embryonic HE, primarily localized in the dorsal aorta, can efficiently give rise to HSCs. The spatiotemporal difference in emergence suggests that HE cells from distinct waves are intrinsically

A full list of affiliations appears at the end of the paper. 🖂 e-mail: Michael.Lie-a-ling@cruk.manchester.ac.uk; Georges.Lacaud@cruk.manchester.ac.uk

different, leading to divergent molecular dependencies. Indeed, NOTCH signaling is essential for HSC development but not for EMP generation^{22,23}. Conversely, *Ezh2* is essential for the generation of functional EMPs, whereas it is dispensable for AGM HSC development^{24,25}.

Single-cell RNA sequencing (scRNA-seq) is ideally suited to identify intrinsic differences between rare cell populations. We previously characterized a granular full-length (Smart-seq2) single-cell transcriptomic profile of the AGM EHT trajectory, defining a HE continuum (HE^{AGM}) encompassing HE cells at various stages of commitment²⁶. Here, we present the acquisition and analysis of a complementary full-length transcriptome of extra-embryonic EHT populations. We identified two distinct extra-embryonic HE populations, both residing within the *RunxI*^{pos}KIT^{pos} endothelial population. The first, HE^{YSP}, is contained within CD24^{neg} *Vwf*^{neg} LYVE1^{pos} endothelial cells, is dominant before E9.5, has EMP potential, and is localized throughout the YS endothelial plexus. The second, HE^{YSA}, is contained within CD24^{pos} *Vwf*^{pos} LYVE^{neg} endothelial cells, is dominant after E9.5, has LMP potential, and is exclusively found in large extra-embryonic arteries.

Our data reveal both striking similarities and differences between extra- and intra-embryonic HE populations. While all HE populations share a common signature marked by the expression of the transcription factors *Gfi1* and *Mycn*, there are pronounced differences with regard to the expression of chromatin modifiers and genes involved in RNA processing. This correlates with increased isoform complexity in the HE^{AGM} transcriptome. Distinct HE^{AGM}-specific isoform expression patterns are observed across a broad range of genes, suggestive of a stochastic transcriptional environment guiding the unique HSPC cell fate choices made within the AGM. Notably, multiple stemness-associated factors, such as *Runx1*, display differential isoform expression profiles when compared to the YS HE populations.

The dataset presented here forms a comprehensive full-length scRNA-seq atlas of three distinct definitive hematopoietic EHT trajectories giving rise, respectively to EMPs, LMPs and HSPCs, which can be accessed and queried at https://shiny.cruk.manchester.ac.uk/AGM YS dataset final/.

Results

Extra-embryonic HE potential resides within the KIT^{pos} population

Although HE activity was previously reported to reside within KIT^{neg} cells in the AGM^{12,27}, it is associated with KIT^{pos} cells during in vitro mouse embryonic stem cell differentiation¹⁶, recapitulating YS hematopoiesis¹⁶. To determine whether extra-embryonic HE is mainly found within the KIT^{neg/low} or KIT^{pos} endothelium (defined as CD31^{pos} and hematopoietic lineage/LIN^{neg}:CD41^{neg}CD45^{neg}TER119^{neg}), we examined the hematopoietic potential of E9.5 and E10.5 YS endothelial cells from Runx1b^{RFP}/Gfi1^{GFP} reporter mice^{26,28,29}. Runx1 and Gfi1 expressions are robust indicators of HE identity^{20,21,26,28}. YS KIT^{neg/low} or KIT^{pos} FACS-sorted single endothelial cells were co-cultured on OP9 cells for 7 days to support EHT and hematopoietic expansion (Fig. 1a and Extended Data Fig. 1a). Hematopoietic potential was only detected in wells seeded with endothelial cells expressing KIT and RUNX1 (Figs. 1b; E9.5 and E10.5). No hematopoietic cells were generated from either the KIT^{pos}Runx1^{neg} or KIT^{neg} endothelial populations. Robust colony formation of the CD41^{neg}CD45^{neg}TER119^{neg}CD31^{pos}KIT^{pos}Runx1b:RFP^{pos} cells was only observed after maturation/EHT on OP9 cells (Fig. 1c and Extended Data Figs. 1a and 2a) indicating that this population contains true HE cells and not already committed hematopoietic cells. Together, these data establish that at E9.5 and E10.5 YS extra-embryonic HE predominantly resides within the KIT^{pos}Runx1^{pos}CD31^{pos}LIN^{neg} population.

scRNA-seq profiling of the extra-embryonic EHT trajectory

To construct a comprehensive full-length Smart-seq2 scRNA-seq dataset capturing the extra-embryonic EHT process, akin to our previous AGM HE study²⁶, we isolated individual cells of extra-embryonic

populations across E9.0, E9.5 and E10.5. These included cells from HE-enriched (FACS-HE) populations from single and double *Runx1* and *Gfi1* reporter mice, non-HE endothelial cells (FACS-ENDO), and committed EMP (FACS_EMP) and LMP (FACS-LMP) hematopoietic progenitors (Fig. 1d and Extended Data Fig. 1a,b). Overall, 960 sequenced cells (100 FACS-ENDO, 660 FACS-HE, 118 EMP and 82 LMP) passed quality control with a median of 6,553 genes detected per individual cell (Extended Data Fig. 2b and Methods).

Unsupervised hierarchical clustering separated the cells into five clusters (K1–K5), with two main dendrogram branches (Fig. 1e). The first branch (K1–K2) exhibits a strong endothelial identity, with K1 containing the majority of FACS-ENDO (Fig. 1e-f). The second branch (K3–K5) has a pronounced hematopoietic identity, with the FACS-EMP and the FACS-LMP cells localizing within K4 and K5, respectively (Fig. 1e,f). K3 also displays a strong hematopoietic profile, including expression of *Ptprc (CD45)* and *Myb*, and markedly reduced expression of endothelial genes (*Cdh5*, *Kdr/Flk1*, *Pecam1* and *Procr*) compared to K1–K2 (Fig. 1e,f). These data indicate that HE cells reside in K2, and that K3 consists of committed early hematopoietic progenitors.

Finally, we reclustered the above YS populations with the addition of 115 YS cells, which were sorted using the established AGM HE phenotype: $KIT^{neg}CD41^{neg}CD45^{neg}CDH5^{pos}Gfil^{Gfilbpos}$ (refs. 21,26). More than 95% of these cells clustered together with FACS-ENDO cells, further confirming that within the YS, HE resides within the KIT^{pos} population (Extended Data Fig. 2c–f). Altogether, these analyses suggest that we captured the full extra-embryonic YS EHT process.

Integration of YS and AGM scRNA-seq data reveals three distinct EHT trajectories

To compare extra-embryonic with intra-embryonic EHT, we conducted a joint analysis with our previously published AGM EHT dataset²⁶ (Extended Data Fig. 3a). We utilized a semi-supervised clustering approach and focused on populations that retain some endothelial characteristics: extra-embryonic clusters K1-K3 and AGM CDH5^{pos} clusters (Fig. 2a,b). The data integration revealed three parallel sets of EHT clusters (Fig. 2b-d) with minimal overlap between extra-embryonic and AGM-derived cells (Fig. 2a,b). We designated the three trajectories as trajectory A and B for the YS-derived cells and trajectory C for the AGM-derived cells. Overall, the integration resulted in 13 clusters (Fig. 2b), which were named based on their known identity/trajectory within the Uniform Manifold Approximation and Projection (UMAP): AGM clusters²⁶ (c1 arterial endothelium, c2 pre-HE, c3 HE, c4 EHT, c5 intra-aortic-hematopoietic-clusters), YS-A trajectory clusters (a1 and a2), YS-B trajectory clusters (b1, b2 and b3), YS-progenitor clusters (p1 and p2). The only cluster that demonstrated an appreciable overlap between YS and AGM-derived cells was called Mix (Fig. 2b). Cells from YS endothelial (K1) and hematopoietic (K3) clusters, respectively, contributed to b1 and p1/p2 populations. Most cells from the YS HE population (K2) contributed to two distinct pairs of clusters (a1-a2 and b2-b3), situated parallel to AGM c3 HE and c4 EHT. Another scRNA-seq profiling study annotated cells similar to c3_HE as pre-HE, and c4_EHT as HE^{26,30}. To reconcile semantic differences in HE definitions across studies, we considered both c3 and c4 as a single HE entity or continuum (HE^{AGM}). Using HE^{AGM} and the coexpression of hematopoietic and endothelial genes (Fig. 2c,d), we inferred that extra-embryonic clusters a1, a2, b2 and b3, likely possess HE properties. Overall, the integration of AGM and extra-embryonic EHT datasets suggests the existence of three distinct EHT trajectories.

Differential spatiotemporal emergence of extra-embryonic EHT trajectories

To unravel the characteristics of the extra-embryonic EHT clusters, we first examined the relative prevalence of each cluster present in the FACS-HE population from E9.0 to E10.5 (Figs. 1d-f and 2e). Cells in clusters b2-b3 were more prevalent at earlier (E9.0) developmental

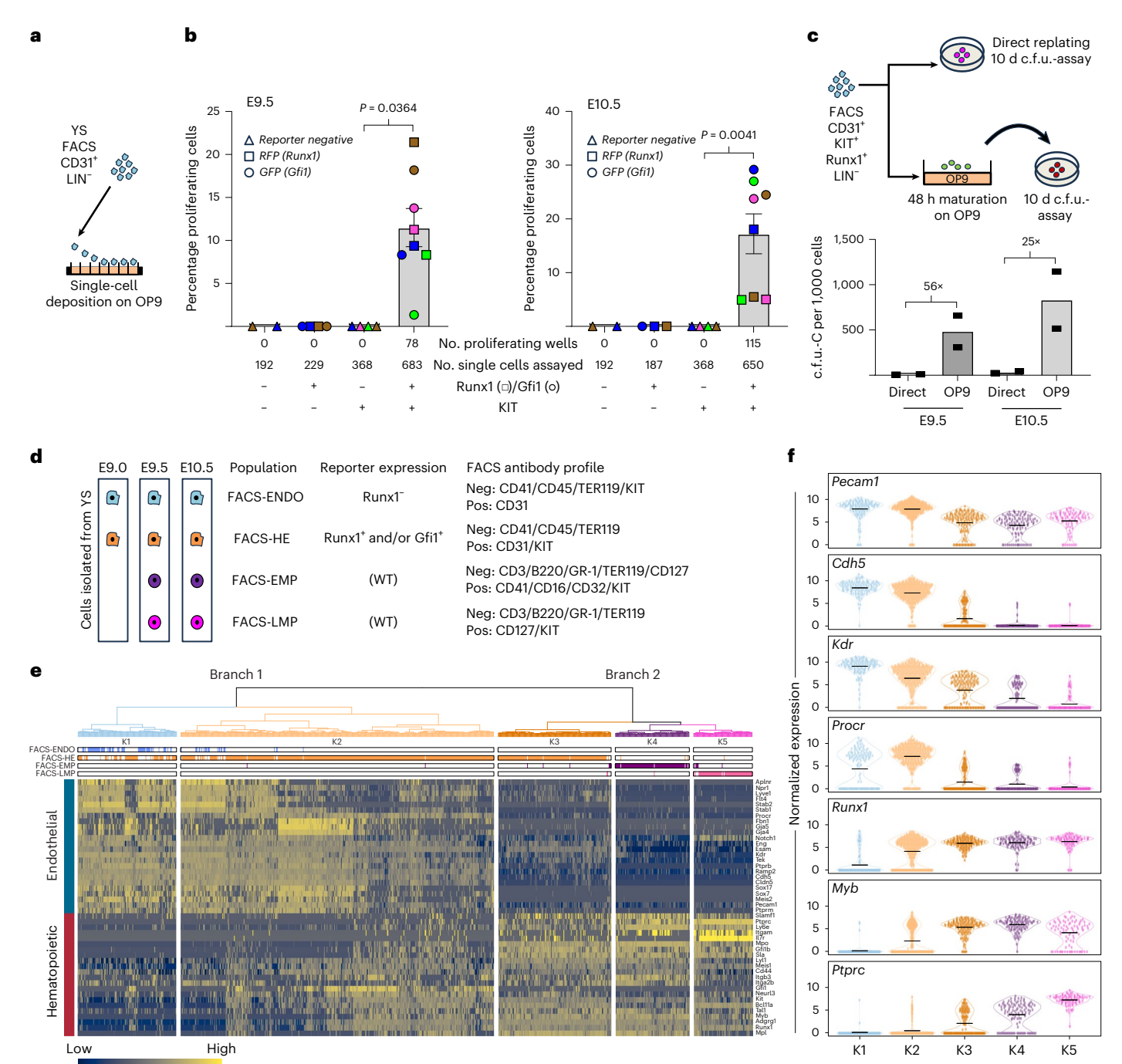


Fig. 1 | Single-cell profiling of the extra-embryonic KIT^{pos} endothelial fraction to characterize extra-embryonic EHT. a-c, Extra-embryonic HE potential resides within the KIT^{pos} population. Schematic of single-cell hematopoietic assays on the CD31^{pos}Lineage^{neg} (CD41^{neg}CD45^{neg}TER119^{neg}) extra-embryonic populations (a). Sorted KIT^{pos} and KIT^{neg} extra-embryonic single cells were co-cultured on OP9 feeder cells for 7 days. Hematopoietic activity was only observed in KIT^{pos}RUNX1^{pos} and KIT^{pos}RUNX1^{pos}GFI1^{pos} cells (b). No hematopoietic activity was observed in either the KIT {\rm ^{pos}RUNX1^{neg}} or the KIT {\rm ^{neg}RUNX1^{pos}} cells. Squares represent Runx1 positive cells isolated from Runx1:RFP reporters, circles represent Runx1/Gfi1 double positive cells isolated from Runx1:RFP/GFi1:GFP double reporters, triangle indicate Runx1/Gfi1 negative cells. Different biological experiments (for each reporter used) are indicated by color (brown, blue, green, magenta). KIT pos cells were obtained from n = 4 biological experiments, KIT neg cells were obtained from n = 2 biological experiments. Bars represent the average percentage of proliferating cells ± s.e.m. Statistical test was a two-tailed paired t-test. Error bars are not displayed for reporter KIT^{neg} samples and these samples were not tested for statistical significance. Hematopoietic colony-forming unit

(c.f.u.) assay on KIT^{pos}Runx1^{pos}CD31^{pos}Lin^{neg} (CD41^{neg}CD45^{neg}TER119^{neg}) extraembryonic cells (c). Cells were either directly replated or co-cultured with OP9 feeder cells for 48 h before replating. Hematopoietic colonies were quantified after 10 days. n = 2 biological experiments. Bars represent the average number of c.f.u. per 1000 cells seeded. Numbers above the bars represent the fold increase in hematopoietic output. **d-f**, Single-cell profiling of extra-embryonic EHT. Schematic of the cell populations FACS sorted from dissected E9, E9.5 and E10.5 YS and processed for full-length single-cell Smart-seq2 RNA sequencing (d). Endo, endothelium. Tree dendrogram generated by hierarchical clustering of the sorted populations in c (e). Two main branches are identified (K1-K2 and K3-K5). Below the dendrogram, the contribution of the different FACS-sorted populations to each cluster is shown. Bottom: heatmap depicting the expression of endothelial (top) and hematopoietic (bottom) genes across clusters K1-K5. Violin plots depicting the expression of selected endothelial (Pecam1, Cdh5, Kdr and Procr) and hematopoietic genes (Runx1, Myb and Ptprc) across clusters K1-K5 (f). Black bars represent the mean expression level.

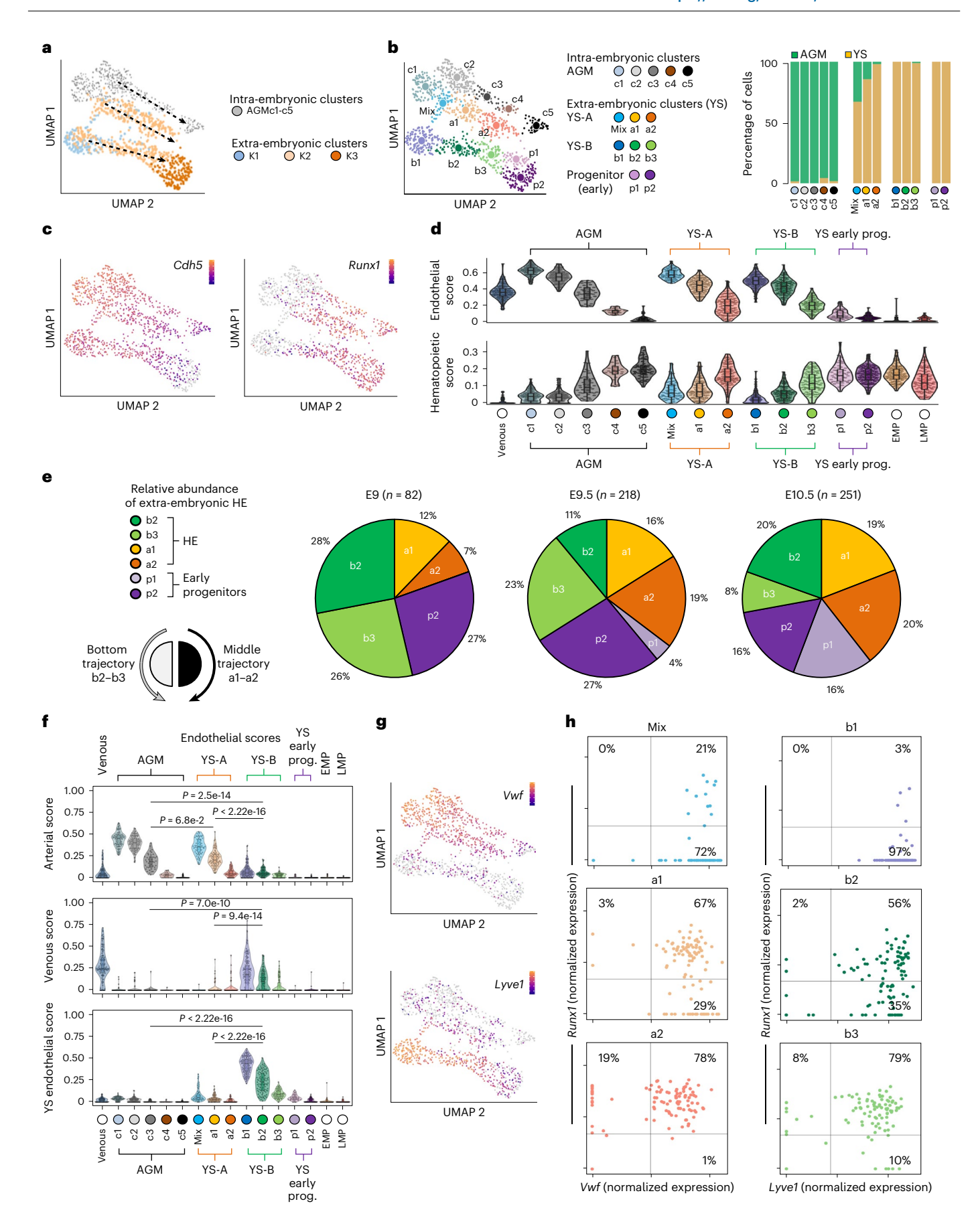


Fig. 2 | Two extra-embryonic EHT trajectories with distinct endothelial **signatures.** Semi-supervised clustering of intra-embryonic (AGM-derived) and extra-embryonic EHT scRNA-seq datasets. a, UMAP of the integrated data overlayed with the K1-K3 extra-embryonic YS clusters defined in Fig. 1d. Arrows indicate the presence of three EHT trajectories (one AGM trajectory and two YS trajectories) b, UMAP of the integrated data depicting the 13 clusters spread across intra-embryonic (AGM-derived) and extra-embryonic cells (YS-derived) cells (left). Clusters AGMc 3 and AGMc 4 form the intra-embryonic/AGM HE continuum (HE^{AGM}). There are two putative HE continua in the extra-embryonic space: YSc_a1, YSc_a2 and YSc_b2, YSc_b3. Graph depicting the contribution of intra-embryonic derived cells (AGM) and extra-embryonic derived cells (YS) to each cluster (right). c, UMAPs depicting the expression of the endothelial gene Cdh5 and the hematopoietic gene Runx1. d, Violin plot depicting endothelial (top) and hematopoietic (bottom) signature scores across all 13 clusters defined in b. The signature scores were calculated using the genes depicted in Fig. 1d. Embedded boxplots indicate the median (horizontal line), the upper and lower hinges represent the 75th and 25th percentile and whiskers extend

to 1.5 × interquartile range. e, Relative abundance of extra-embryonic clusters YSc-b2 YSc-b3, YSc-a1 YSc-a2 (putative HE) and YSc-p1, YSc p2 (early hematopoietic progenitors). Numbers depict the percentage of the total number FACS-HE cells across all analyzed clusters at each embryonic stage. f, Violin plots depicting arterial, venous and YS endothelial scores across all clusters defined in **b**. For reference, AGM-derived venous endothelial cells (left column) and extra-embryonic-derived EMP and LMP populations (right columns) are also included. Embedded boxplots indicate the median (horizontal line), the upper and lower hinges represent the 75th and 25th percentile and whiskers extend to 1.5 × interquartile range. Two-sided Wilcoxon rank-sum tests were used (with P values adjusted via the Benjamini-Hochberg procedure to control the FDR) to compare the early HE clusters (c3, a1 and b2). g, UMAPs depicting the expression of the Vwf (marking the AGM and YS-A clusters) and Lyve1 (marking YS-B clusters), h. Correlation between transcript expression of Runx1 and Vwf in clusters mix, a1 and a2 (YS-A trajectory) (top). Correlation between Runx1 and Lyve1 transcript expression in clusters b1, b2 and b3 (YS-B trajectory) (bottom).

stages than cells in a1–a2, suggesting that the YS-B EHT trajectory is established before the YS-A trajectory. The appearance of the two extra-embryonic progenitor clusters followed a similar sequential pattern, with p2 preceding p1.

As endothelial gene expression plays a pivotal role in defining HE identity, we evaluated whether the different trajectories could be segregated based on endothelial profiles (arterial, venous and YS) (Fig. 2f and Supplementary Table 1). The AGM EHT trajectory exhibited a robust arterial endothelial identity, similar to extra-embryonic clusters mix, a1 and a2, whereas b1, b2 and b3 displayed venous and especially YS endothelial profiles (Fig. 2f). Mix and b1 likely represent non-HE endothelial cells, as they display the strongest arterial and YS endothelial profiles within their respective trajectories while also lacking <code>Runx1</code> expression in most of the cells that make up the cluster (Fig. 2c, f and Extended Data Fig. 3b).

Finally, we screened for specific markers allowing us to determine the spatial localization, within the YS, of cells representing these different EHT trajectories. Differential gene expression analysis identified the endothelial genes *Vwf* (Von Willebrand factor) and *CD24a* (a glycosylphosphatidylinositol (GPI)-anchored cell surface protein) as good markers for the YS-A trajectory. Lyve1 (lymphatic vessel endothelial hyaluronan receptor 1) was associated with the YS-B trajectory (Fig. 2g,h and Extended Data Fig. 3c). Whole-mount staining of E9.5 and E10.5 YS, obtained from a Vwf^{eGFP} reporter³¹ mouse model, for RUNX1, LYVE1 and eGFP revealed their distinct spatial expression patterns within the extra-embryonic vasculature. While high LYVE1 expression was evident throughout the YS plexus and in large veins, eGFP (Vwf expression) staining was confined to large arterial vessels (Fig. 3a,b). Additionally, putative HE cells expressing both RUNX1 and Vwf were primarily observed in large arteries and infrequently in large veins. In the plexus RUNX1pos Vwfpos cells were absent at E9.5 and infrequent at E10.5. Putative HE cells expressing RUNX1 and LYVE1 were distributed throughout the plexus (Fig. 3c-e). Altogether, these results suggest the presence of two separate extra-embryonic HE populations.

The first (b2 and b3) is LYVE1 positive, dominant until E9.5 and can be found throughout the YS endothelial plexus. The second population (a1 and a2) expresses CD24a and *Vwf*, is prevalent after E9.5 and is found in large extra-embryonic arteries.

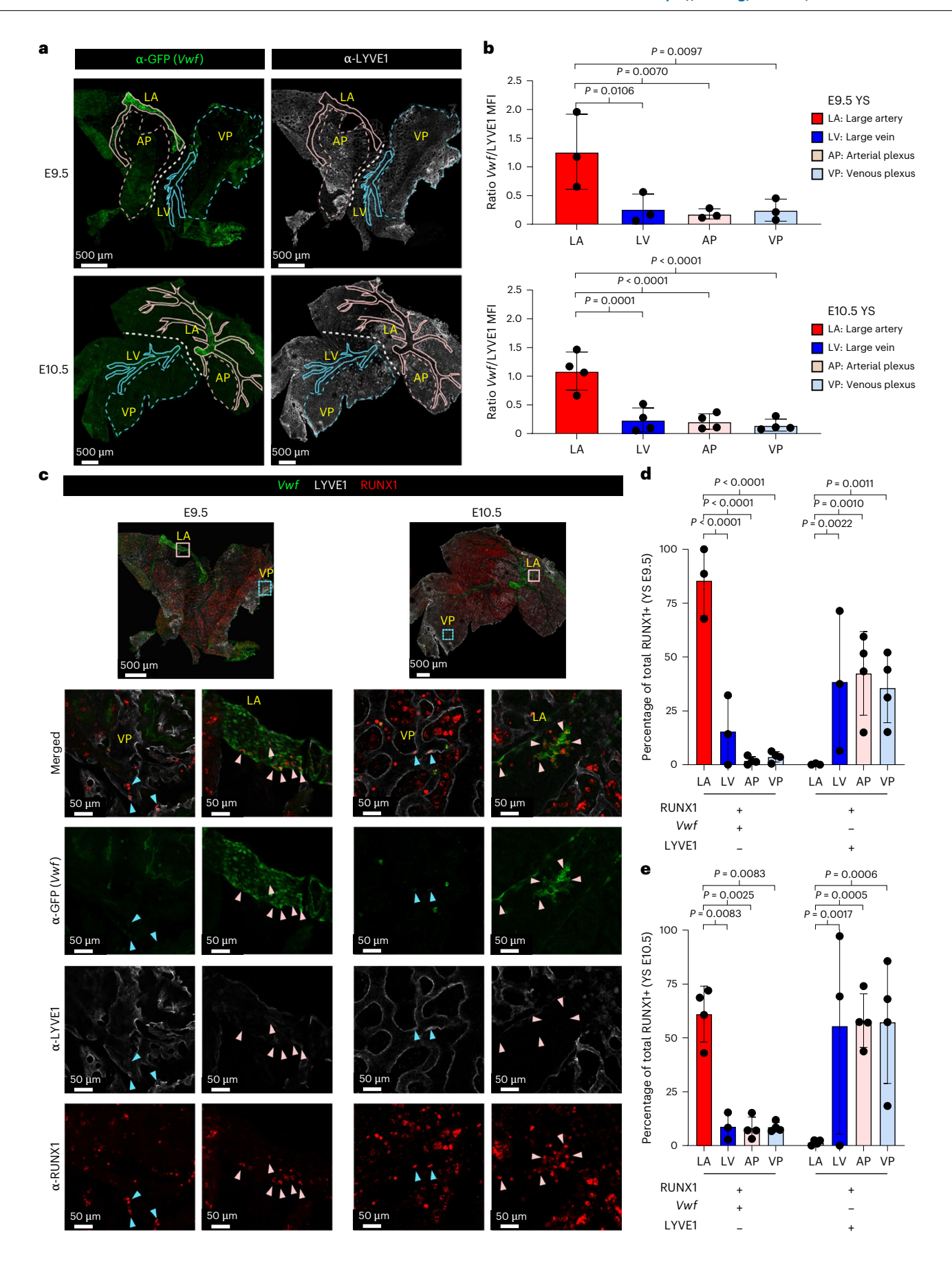
The two extra-embryonic HE populations have distinct hematopoietic potentials

To isolate and functionally characterize the two extra-embryonic HE populations, we screened our data for cell surface markers suitable for FACS enrichment from wild-type (WT) embryos devoid of fluorescent reporters. This highlighted the previously identified Lyve1 and CD24a, as potential markers for respectively the YS-B and YS-A HE trajectory. Mcam (melanoma cell adhesion molecule) was expressed at early stages of both trajectories (Fig. 4a,b and Extended Data Fig. 3b,c). Next, we examined by flow cytometry Runx1^{RFP} expression, a strong indicator of HE identity, in extra-embryonic KIT^{pos}CD31^{pos}LIN^{neg} YS endothelial subpopulations defined by a combination of these markers: LYVE1^{neg}CD24^{pos}MCAM^{pos}, LYVE1^{neg}CD24^{pos}MCAM^{neg}, LYVE1^{pos}CD24^{neg} MCAM^{pos} and LYVE1^{pos}CD24^{neg}MCAM^{neg}. Within the MCAM^{pos} cell populations, few cells displayed transcription of the *Runx1* locus (RFP 1.5–23%), suggesting limited HE enrichment. In contrast, both MCAM^{neg} populations were highly enriched for cells with an active Runx1 locus (CD24^{pos}LYVE1^{neg}MCAM^{neg} 72 – 88% and CD24^{neg}LYVE1^{pos} MCAM^{neg} 62-67%) (Fig. 4c). Subsequent scRNA-seq of cells in these populations confirmed that these MCAM^{neg} populations are enriched for the extra-embryonic HE (Fig. 4d).

To functionally assess the hematopoietic potential of the two YS HE populations, single cells were sorted, co-cultured on OP9, and evaluated for myeloid (GR1, MAC1/CD11b), erythroid (TER119) and lymphoid (CD19) potential by flow cytometry after 14 days of co-culture. Single cells from both YS HE populations displayed hematopoietic activity regardless of the developmental stage (Fig. 4e). Wells seeded with CD24^{pos} cells contained myeloid, lymphoid and mixed lymphoid/myeloid cells, whereas wells seeded with LYVE1^{pos} cells predominantly

Fig. 3 | **Spatial separation between transcriptomically different EHT trajectories in the yolk sac. a**, Confocal whole-mount immunofluorescence (WM IF) analysis of E9.5 (top) and E10.5 (bottom) Vw_f^{eGFP} YS. Images show maximum intensity three-dimensional (3D) projections. Representative areas where fluorescence has been quantified are delimited by lines. Pink solid line, large artery (LA); turquoise solid line, large vein (LV); pink dashed line, arterial plexus (AP); turquoise dashed line, vein plexus (VP). Scale bars, 500 μm. **b**, The ratio of Vw_f -associated MFI to LYVE1-associated MFI is plotted on the y axis, reflecting the relative fluorescence intensities within selected areas in Vw_f -GFP YS as displayed in Fig. 3a. n = 3 E9.5 and n = 4 E10.5 YS were analyzed (6–10 areas per YS). Error bars represent mean \pm s.d. Statistical test used was a one-way analysis of variance (ANOVA) (Fisher's least significant difference).

c, WM IF analysis of E9.5 (left) and E10.5 (right) $\it Vwf^{\rm GGFP}$ YS. Whole YS images show maximum intensity 3D projections. The boxed area in the merged image is magnified in the lower panel and shows a single 2.5-mm-thick optical slice. Turquoise arrowheads indicate RUNX1 $^{\rm pos}\it Vwf^{\rm pos}\it LYVE1^{\rm pos}$ putative HE cells; pink arrowheads indicate RUNX1 $^{\rm pos}\it Vwf^{\rm pos}\it LYVE1^{\rm neg}$ putative HE cells. Scale bars, 500 µm (3D), 50 µm (slice). **d,e**, Quantification of the percentage of RUNX1 $^{\rm pos}\it Vwf^{\rm pos}\it LYVE1^{\rm neg}$ and RUNX1 $^{\rm pos}\it Vwf^{\rm pos}\it LYVE1^{\rm pos}$ cells on the total of RUNX1 positive cells in LA, LV, AP and VP of E9.5 (**d**) and E10.5 (**e**) $\it Vwf^{\rm eGFP}\it YS$ (displayed in Fig. 3c). Each dot represents measurements from an individual YS. E9.5 LA and LV $\it n=3$, AP and VP $\it n=4$. E10.5 LV $\it n=3$, LA, AP and VP $\it n=4$ 5-17 areas per YS were analyzed. Error bars represent mean $\it \pm s$.d. Statistical test used was a two-way ANOVA (Fisher's least significant difference).



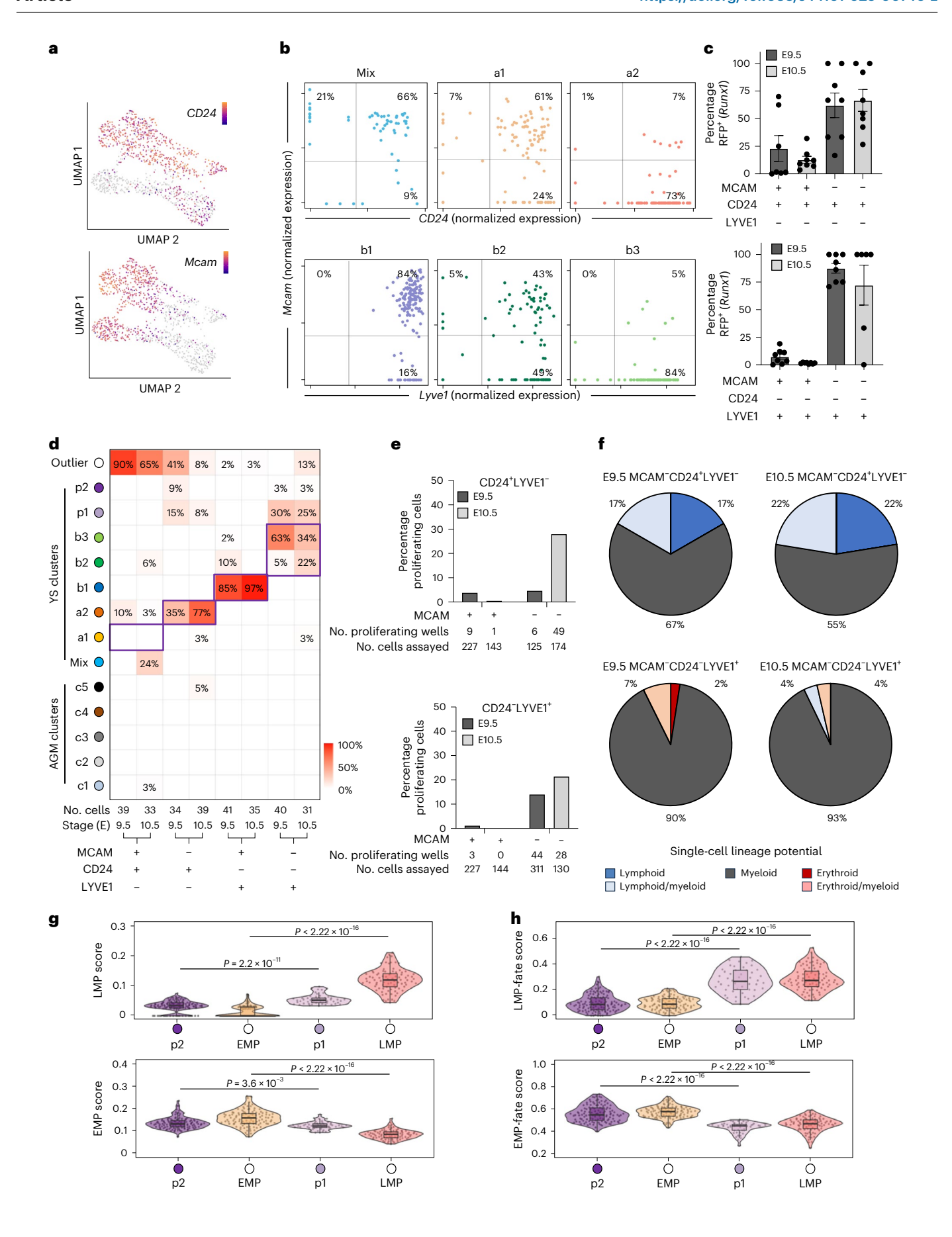


Fig. 4 | CD24^{pos} YS HE has lymphoid-myeloid potential and LYVE1^{pos} YS HE has erythroid-myeloid potential. a, UMAPs depicting the expression of Cd24a (marking the AGM and YS-A clusters) and Mcam (marking cells toward the endothelial end of all three trajectories). **b**, Correlation between Cd24a and Mcam, transcript expression in clusters mix, a1 and a2 (YS-A trajectory) (top). Correlation between Lyve1 and Mcam, transcript expression in clusters b1, b2 and b3 (YS-B trajectory) (bottom). c, Flow cytometry on extra-embryonic CD45^{neg}CD41^{neg}TER119^{neg} (Lineage negative) CD31^{pos}KIT^{pos} cells from Runx1:RFP reporter embryos. MCAM, LYVE1 and CD24 antibodies were used to analyze the proportion of Runx1 (RFP) expressing cells in different subpopulations. Each dot represents cells from a single YS. E9.5 $MCAM^{pos}CD24^{pos}LYVE1^{neg}$ n = 7, $E10.5 MCAM^{neg}CD24^{neg}LYVE1^{pos}$ n = 6, all other samples n = 8. Bars represent the average \pm s.e.m. **d**. Heatmap displaying the distribution (as percentage) of different CD45^{neg}CD41^{neg}TER119^{neg}CD31^{pos}KIT^{pos} FACS-sorted, scRNA-sequenced cell populations across the in silico EHT clusters defined in Fig. 2b. Based on *k*-nearest-neighbor classifier approach. MCAM, LYVE1, CD24 sorting profiles are depicted on the x axis. Purple boxes indicate the expected/predicted cluster (y axis) for the sorted population (x axis) based on the data presented in Fig. 4b. e, Single-cell hematopoietic assays of YS-A HE (KITPOSCD31POSLINnegLYVE1negCD24POSMCAMneg) and YS-B HE (KIT^{pos}CD31^{pos}LIN^{neg}LYVE1^{pos}CD24^{neg}MCAM^{neg}) cultured on OP9 feeder cells for

14 days. The percentage of wells with proliferating hematopoietic cells is shown. f, Lineage distribution of the hematopoietic cells shown in e as determined by flow cytometry for myeloid (GR1 and MAC1/CD11b), erythroid (TER119) and lymphoid (CD19) markers. g, Violin plots depicting LMP (top) and EMP (bottom) scores across early progenitor clusters p1 and p2. EMP and LM signatures have been previously published and are listed in Supplementary Table 1. Embedded boxplots indicate the median (horizontal line), the upper and lower hinges represent the 75th and 25th percentile and whiskers extend to 1.5 × interquartile range. Two-sided Wilcoxon rank-sum tests were used (with P values adjusted via the Benjamini-Hochberg procedure to control the FDR) to compare EMP and LMP as well as clusters p1 and p2. h, Violin plots depicting prospective LMP fate (top) and EMP fate (bottom) scores across early progenitor clusters p1 and p2 as well as EMP and LMP populations. EMP fate (8 genes) and LMP fate (14 genes) signatures (Supplementary Table 1) were extracted by intersecting pairwise differential gene expression results (EMP versus LMP and P1 versus P2; Extended Data Fig. 3f). Embedded boxplots indicate the median (horizontal line), the $upper and \ lower \ hinges \ represent \ the \ 75 th \ and \ 25 th \ percentile \ and \ whiskers$ extend to 1.5 × interquartile range. Two-sided Wilcoxon rank-sum tests were used (with P values adjusted via the Benjamini-Hochberg procedure to control the FDR) to compare EMPs and LMPs as well as clusters p1 and p2.

gave rise to myeloid, erythroid and erythroid/myeloid cells (Fig. 4f). We also utilized our Runx1b^{RFP} reporter model in conjunction with this HE marker panel to enrich for the least progressed MCAM^{pos} endothelial cells within the YS-A (a1, LYVE1^{neg}CD24^{pos}MCAM^{pos}Runx1RFP^{pos}) and YS-B (b2, LYVE1^{pos}CD24^{neg}MCAM^{pos}Runx1RFP^{pos}) trajectories. The hematopoietic potential of both MCAM^{pos} cell populations was lower than that of the respective MCAM^{neg} populations (Fig. 4e and Extended Data Fig. 3d,e), but the hematopoietic identity of the output was similar (Fig. 4f and Extended Data Fig. 3d,e).

Finally, as the emergence of the lymphomyeloid-producing HE clusters a1-a2 and the erythromyeloid-producing HE cluster b2-b3 closely correlated with the emergence of respectively cluster p1 and p2 (Fig. 2e), we investigated whether these two progenitor populations show signs of early LMP or EMP commitment based on previously published EMP and LMP gene signatures (Fig. 4g and Supplementary Table 1). Although these signatures could distinguish p1 (which resembled EMP) from p2 (which resembled LMP) the difference between the two progenitor populations was minimal (Fig. 4g). This prompted us to investigate if we could define a more powerful gene signature to identify early EMP and LMP potential during progenitor emergence. We used the intersection of pairwise differential gene expression analysis (LMP versus EMP and p1 versus p2) to extract prospective EMP fate and LMP fate signatures (Supplementary Table 1 and Extended Data Fig. 3f). These 'fate' signatures performed better at assigning p1 to an LMP and p2 to an EMP fate (Fig. 4h), suggesting that these gene signatures could be useful to determine whether early progenitors have an EMP or LMP fate.

Overall, these results demonstrate that the two extra-embryonic HE populations associate with wave 2 EMP and LMP production,

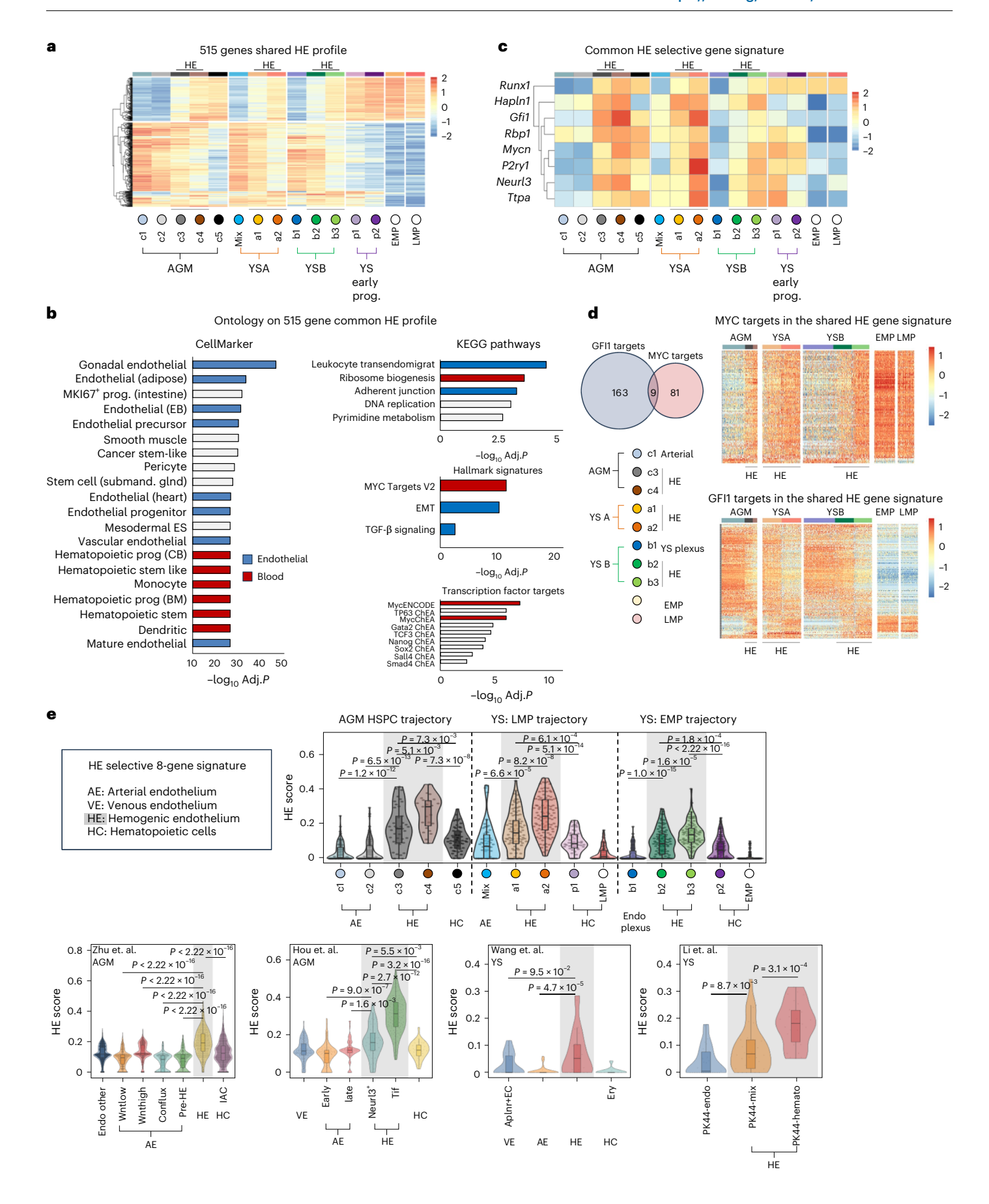
a finding consistent with their distinct endothelial identities and temporal abundance 32 . Given these findings, we hereafter named the three different HE populations based on their distinct localizations; HE $^{\text{AGM}}$ (clusters c3–c4), HE $^{\text{YSA}}$ /clusters a1–a2, which are found within the YS arteries, HE $^{\text{YSP}}$ /clusters b2–b3 which are found within the YS endothelial plexus.

Identification of a shared common HE signature marked by *Gfi1* and *Mycn*

Next, we used the three HE transcriptomes to identify shared HE and EHT characteristics. Acknowledging the continuous nature of the EHT process and the hybrid endothelial-hematopoietic identity of the HE, we identified shared differentially expressed genes (DEGs) between the three HE populations and the extremities (non-HE endothelium and the EMP/LMP populations) of the EHT trajectory (Extended Data Fig. 4a and Supplementary Table 2a). The resulting 515 genes profile is a hybrid of genes expressed in endothelial cells (330 of 515) and genes expressed in hematopoietic cells (178 of 515) (Fig. 5a and Supplementary Table 2a). It contains many genes, including Proc, Neurl3, Runx1 and Gfi1 previously associated with an HE identity (Supplementary Table 2a). Ontology analyses revealed enrichments for categories typically associated with HE and EHT including EMT, TGF-β signaling³³ and ribosome biogenesis (Fig. 5b). Notably, just 7 out of the 515 genes displayed a distinct HE-restricted expression pattern: Neurl3, Hapln1, Rbp1, Ttpa, P2ry1 and the transcription factors Gfi1 and Mycn (Fig. 5c). Almost half (49%, 253 genes) of the genes within the shared profile could be identified as potential targets of these two transcription factors (Fig. 5d and Supplementary Table 2a,b). Most of the potential MYC

Fig. 5| **The shared common HE signature is marked by the transcription factors** *Gfi1* **and** *Mycn.* **a**, Heatmap depicting the relative expression of all the 515 genes in the shared common profile across intra- and extra- embryonic EHT trajectories (as defined in Fig. 2b). All HE populations display a mixed expression of genes that are strongly expressed in either the endothelial or hematopoietic arms of the EHT trajectory. YS-derived EMPs and LMPs are included for reference (right). **b**, Gene Ontology analysis of the 515 gene universal HE profile. Top Gene Ontology hits (capped at 20) from the CellMarker, KEGG, Hallmark and ChEA/ENCODE databases are shown. Adjusted *P* values were calculated using Fisher's exact test with Benjamini–Hochberg correction **c**, Heatmap depicting the relative expression of all seven HE-selective genes within the shared HE profile and *Runx1* across all three EHT trajectories (as defined in Fig. 2b). YS-derived EMPs and LMPs are included for reference (right columns). **d**, The shared HE profile contains many GFI1 and MYCN target genes. Intersect of GFI and MYCN

target genes in the universal HE profile (left). Single-cell heatmaps depicting the expression of shared HE profile MYCN target genes (top) and GFII target genes (bottom) across intra- and extra- embryonic HE populations (right). e, Violin plots demonstrating that the HE signature defined in Fig. 5c effectively identifies HE cells in all three EHT trajectories analyzed in this manuscript (top) 26 as well as in previously published AGM and YS datasets (bottom) $^{30,36-38}$. Where appropriate the y axis of the plots shows the names of the population/cluster nomenclature used in the relevant publications. AE, arterial endothelium; HC, hematopoietic cell. Embedded boxplots indicate the median (horizontal line), the upper and lower hinges represent the 75th and 25th percentile and whiskers extend to $1.5 \times$ the interquartile range. Two-sided Wilcoxon rank-sum tests were used (with *P* values adjusted via the Benjamini–Hochberg procedure to control the FDR) to compare relevant populations.



target genes displayed increased expression toward the hematopoietic end of the three HE. Conversely, most of the GFI1 targets 21,34,35 were downregulated toward the hematopoietic end (Fig. 5d and Supplementary Table 2a,b). Finally, we verified that the seven HE-restricted genes in combination with Runx1 can be used as an eight-gene HE-selective gene signature to identify cells with HE characteristics across independent mouse intra-embryonic (AGM) 26,30,36 and extra-embryonic (YS) 37,38 scRNA-seq EHT datasets (Fig. 5e).

Overall, we established a shared HE profile that encompasses an eight-gene HE signature that is sufficient to identify cells with HE characteristics. Furthermore, *Gfil* and *Mycn* are the only transcription factors with a HE-restricted expression pattern.

Chromatin modifiers and splicing machinery are differentially expressed between intra- and extra-embryonic HE

To identify differences between the three HE populations, we conducted pairwise differential expression analyses; HE^{AGM} versus HE^{YSA}, HE^{AGM} versus HE^{YSP} and HE^{YSA} versus HE^{YSP} (Fig. 6a, Extended Data Fig. 4b,c and Supplementary Table 3a). Genes significantly upregulated in HE^{YSP} exhibited a distinct (myeloid and erythroid) hematopoietic identity (Extended Data Fig. 5a) with some myeloid genes already expressed within the non-HE YS endothelium (Extended Data Fig. 5b,c and Supplementary Table 3b). Genes significantly upregulated in the other two HE populations did not display a similarly overt hematopoietic signature (Extended Data Fig. 5a and Supplementary Table 3b). HE^{YSA} most closely resembled HE^{AGM} (Extended Data Fig. 4c and Supplementary Table 3a) with the notable expression of Notch pathway components in both the HE^{AGM} and the HE^{YSA} consistent with their arterial identity (Extended Data Fig. 5d)³⁹.

Overall, HE^{AGM} contained a large group of genes that were more highly expressed compared to one or both extra-embryonic HE (Fig. 6a, Extended Data Fig. 4c and Supplementary Table 3a). Gene Ontology analysis identified two main functionalities within these HE^{AGM} selective genes; chromatin modification and RNA processing/splicing (Fig. 6b and Supplementary Table 3a–c). Specifically, 28 genes related to chromatin modification (Extended Data Fig. 6a) and 49 RNA processing genes (Fig. 6a) demonstrated a $\geq 1.5 \log_2$ fold change (FC) in HE^{AGM} over at least one of the extra-embryonic HE populations (Supplementary Table 3a–c).

The HE^{AGM}-specific upregulation of RNA processing genes is in line with a recent study describing changes in RNA transcript diversity during AGM EHT⁴⁰. Indeed, we observed HE^{AGM}-specific upregulation of genes encoding the splice site recognition proteins SRSF1, SRSF2 and SRSF9, implicated in changes in transcript diversity observed during EHT in the AGM⁴⁰ (Fig. 6c and Supplementary Table 3a). The most differentially expressed RNA processing factors included *Psip1*, encoding a SRSF1 interacting protein, *Hnrnp1*, an activator/repressor of

Fig. 6 | Differential expression of chromatin modifiers and splicing machinery between intra- and extra-embryonic HE correlates with distinct isoform expression landscapes. a, Venn diagram depicting the result of pairwise DEG analysis on HEAGM, HEYSA and HEYSP (top). 'Up' indicates a gene is upregulated (log₂FC > 1.5) versus at least one other HE population. Single-cell heatmap depicting the genes from GO: RNAsplicing_GO_0008380 that are differentially expressed between the HE populations (bottom). b, Gene Ontology analysis (GO cellular components) on genes that are differentially expressed between HE^{AGM} and YS HE (log₂FC > 1.5 higher expression). Adjusted P values were calculated using Fisher's exact test with Benjamini-Hochberg correction c, Violin plots depicting the expression of selected RNA processing genes across HE^{AGM}, HE^{YSA} and HE^{YSP}. Arterial endothelium and plexus endothelium are shown for reference. d, Analyses of isoform entropy difference between HEAGM versus $HE^{YSP}, HE^{AGM} versus \, HE^{YSA} \, and \, HE^{YSP} \, versus \, HE^{YSA}. \, Scatter-plots \, showing \, the \, SCATTER \, and \,$ genes having differential usage pattern for the indicated comparison (left). Black dots represent genes with significant mean entropy differences (mean difference > 0.1, FDR Padj < 0.05). Statistical test Wilcoxon signed-rank test, two-tailed. Gray dots represent genes with nonsignificant changes. Bar graphs

exon inclusion, and *Casc3*, which functions in the non-sense-mediated decay pathway (Fig. 6c and Supplementary Table 3c).

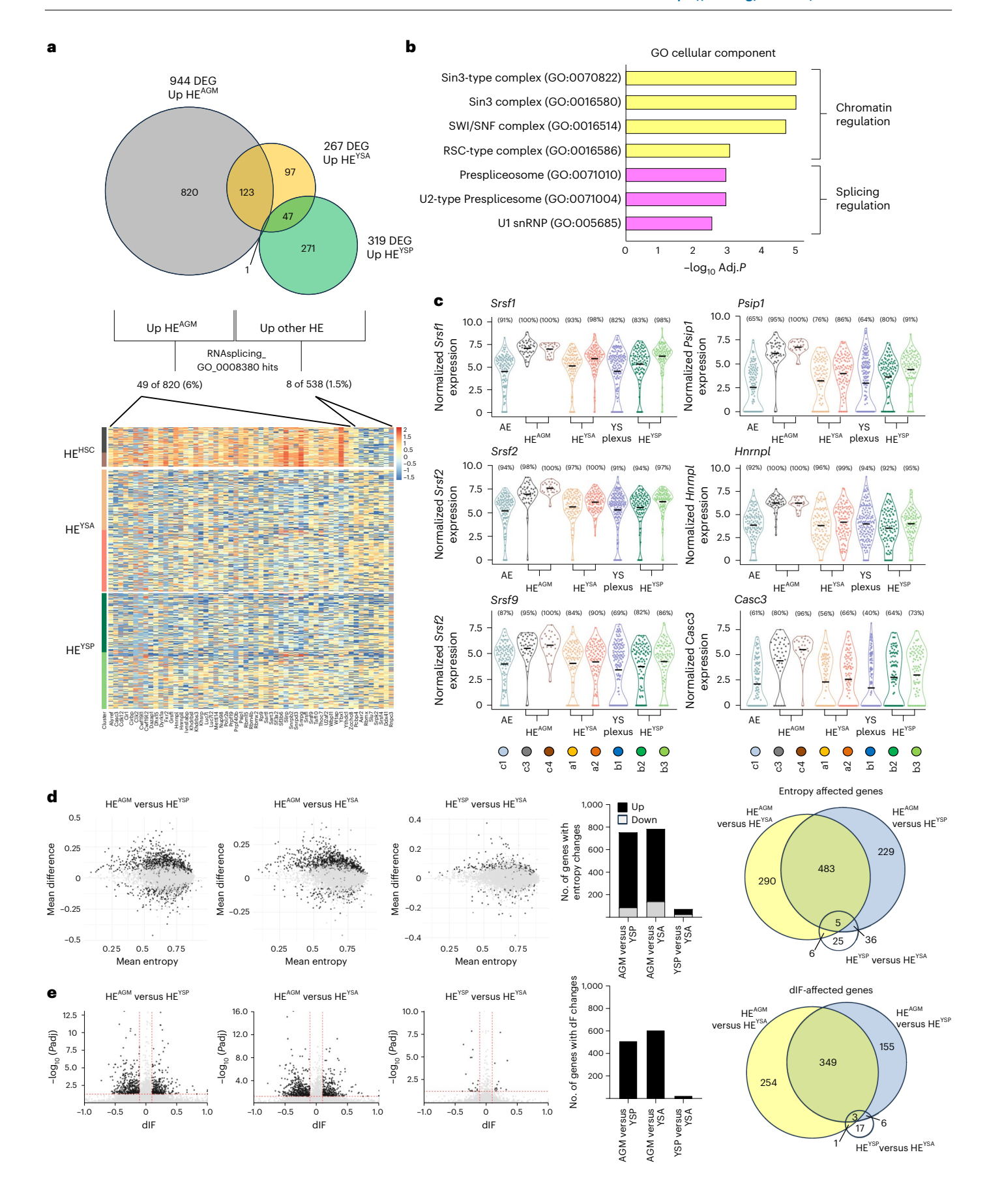
Overall, these analyses reveal that the HE^{YSP} has a distinct hematopoietic profile. Furthermore, HE^{AGM} displays a unique gene expression profile, not observed in either YS HE, characterized by higher expression levels of chromatin modifiers and spliceosome components.

HE^{AGM} transcriptome displays a higher isoform complexity compared to extra-embryonic HE populations

The increased expression level of splicing-related genes in HEAGM suggests that this HE has a distinct isoform expression landscape compared to the YS HE populations. To assess this, we queried our Smart-seq2 dataset at the isoform level. To interrogate differences in isoform expression patterns on a gene level we calculated changes in gene entropy (mean Laplace entropy difference) and dIF (difference in isoform fraction) between the three HE populations 41,42. In this context increased entropy represents a shift toward a higher transcriptome complexity (more balanced expression of multiple isoforms), while dIF calculations detect shifts in the dominant isoform expressed from a given locus (Extended data Fig. 6b). Both these metrics highlighted a prominent difference in the isoform landscape in the AGM HE compared to both YS HE populations (Fig. 6d,e and Supplementary Table 4a-d). In contrast only minor differences were observed in between the two YS HE populations (Fig. 6d-e and Supplementary Table 4a-d). A total of 1,049 gene loci showed significant differences in entropy (Fig. 6d) compared to one or both YS HE populations. Furthermore, the vast majority (84%) of these gene loci showed increased entropy values in HE^{AGM} compared to the YS HE populations. In contrast, entropy differences were found in only 72 gene loci when the two YS HE were compared to each other. with 64% showing increased entropy within the HEYSP when compared to HEYSA. Analysis of dIF changes (Fig. 6e) gave similar results with a large set of genes (768) showing significant shifts in dominant isoform expression when comparing HE^{AGM} to one or both YS HE populations. 46% of these genes had different dIF values compared to both HEYSA and HE^{YSP}. Only a small set of 27 genes displayed significant dIF differences between the YS HE populations.

Collectively, 1,597 genes exhibited isoform level differences between HE^{AGM} and one or both extra-embryonic HE populations. This gene set included a substantial fraction of genes not detected by standard differential gene expression analyses (Fig. 7a left and Supplementary Table 4a), highlighting that the two methods of analyses capture distinct subsets of potential effector genes. Ontology analyses (Fig. 7a right and Supplementary Table 4e) of the set of 1,597 revealed enrichment of genes involved in basal cellular machineries, including RNA (spliceosome), ribosome and cell cycle-related ontologies. Overall, we found that singular clear shifts from one specific isoform to another were rare, with often multiple different (sized)

depicting the number of genes with differential entropy values in the different comparisons (middle). The proportion of genes with increased and decreased entropy values are depicted in black and gray, respectively. HEAGM is skewed toward genes with higher entropy values (chi-squared goodness of fit test, P < 0.0001). Venn diagram depicting the intersect of the different comparisons (right). Only a very small set of genes shows entropy differences between the HEYSB versus HEYSA. e, Differences in isoform fraction (dIF) analyses between HEAGM versus HEYSA, HEAGM versus HEYSA and HEYSP versus HEYSA. Scatter-plots showing the gene with dIF changes for the indicated comparison (left). Black dots represent genes with significant dIF changes (dIF > 0.1, FDR Padj < 0.05). Statistical test used was the IsoformSwitchAnalyzeR implementation of the differential transcript usage (DTU) test in the satuRn R package (https://f1000research.com/ articles/10-374/v2) (a generalized linear model-based test). Gray dots represent genes with nonsignificant changes. Bar graphs depicting the number of genes with dIF changes in the different comparisons (middle). Venn diagram depicting the intersect of the different comparisons (right). Only a very small set of genes show dIF differences between the HE^{YSP} versus HE^{YSA} .



transcripts (both coding and noncoding) showing subtle shifts in proportions (Supplementary Table 4). Examples (Extended Data Fig. 7a–d) were we observed discernible differential splicing events (defined as, partial or complete, exon inclusion/exclusion changes) between HE^{AGM} and YS HE are *Rpl34*, encoding part of the large 60s ribosomal subunit; Arglu1 a splice modulator; Ythdf2 a m⁶A-dependent RNA degrader; Pfn1, a cytoskeleton modulating protein. Notably, the latter two have been implicated in HSPC biology ^{43,44}. Ontology analyses of the small number of genes affected on an isoform level between HE^{YSP} and HE^{YSM} did not yield robust Gene Ontology results (Extended Data Fig. 6c and Supplementary Table 4e).

Together, these data demonstrate that the increased expression of splicing-related genes in HE^{AGM} correlates with an isoform expression landscape that is distinct from both YS HE populations.

Exclusive expression of Runx1 Δ exon 6 transcripts negatively impacts HSC emergence

To focus on potential drivers of an HSC fate we restricted our analyses to transcription/chromatin factors within the HEAGM isoform list (210/1579; Fig. 7b and Supplementary Table 4a). As with the full list, this sublist also contained a substantial number of candidates not found by differential gene expression or analyses of the shared HE profile (Fig. 7b left and Supplementary Table 4a). Cell-type ontology analyses revealed an enrichment for factors associated with stemness (Fig. 7b middle and Supplementary Table 4e). Most of these factors (24 of 32) displayed differential entropy values (Fig. 7b right and Supplementary Table 4a). The majority of the genes in the entropy category displayed increased entropy values in HE^{AGM} (23 of 24), which precludes the identification of a single dominant differentially expressed isoforms (Supplementary Table 4). A small subset of the genes (n = 8)demonstrated dIF changes. Further screening for isoform differences between HE^{AGM} and both YS HE populations, as well as differential splicing events, highlighted Runx1 as a notable candidate.

Multiple annotated *Runx1* transcripts showed shifts in proportion between the three HE populations (Extended Data Fig. 7e). Overall, there is a mix of distal transcripts (Runx1c and short Runx1c 5' transcripts) and proximal transcripts (Runx1b and short Runx1b 5' transcripts). The pattern of expression suggests the three populations are at different stages of shifting from the earliest expressed isoform, *Runx1b*, toward the late expressed isoform *Runx1c*. The proportion of

full Runx1c transcripts is at its highest in HE^{AGM}, is decreased HE^{YSA} and is at its lowest in HE^{YSP} (Extended Data Fig. 7e, middle). The opposite was observed for short Runx1c 5' transcripts (Extended Data Fig. 7e middle and left). We also observed a small but significant twofold increase in the proportion of Runx1 isoforms lacking exon 6 ($Runx1 \Delta 6$) in HE^{AGM} compared to HE^{YSP} (Extended Data Fig. 7e). The difference between HE^{AGM} and HE^{YSA} was much less obvious suggesting that the shift in $Runx1 \Delta 6$ correlates with an arterial identity of the HE.

Although Runx1c is known to be preferentially expressed in HSCs⁴⁵, previous manipulations of Runx1 isoform expression, by enforcing the expression of only Runx1b transcripts, did not reveal striking effects on the HSC population 46 ; however, the absence of $\Delta 6$ transcripts has been previously associated with reduced numbers of HSPCs, including long-term HSCs (LT HSCs), in the bone marrow of adult mice⁴⁷. Together with our observations this suggest that the Δ6 isoform could potentially impact positively on HSC emergence; however, the specific exclusion of Runx1 exon 6 has not been evaluated in vivo. Therefore, we generated homozygote $Runx1\Delta6$ embryos by CRISPR-Cas9 mediated deletion in mouse zygotes followed by implantation⁴⁸. Analysis of E11.5 YS and AGM regions of these embryos demonstrated a significant reduction of emerging hematopoietic cells (defined as either CD31^{pos}KIT^{pos}CD45^{pos} (Fig. 7c) or KIT^{pos}CD45^{pos} (Extended Data Fig. 7f)) specifically in the AGM regions of $\Delta 6$ embryos, while the YS seemed largely unaffected (Fig. 7c). Furthermore, in $\Delta 6$ embryos we observed significantly less phenotypic LT HSCs within both the E11.5 AGM (CD31^{pos}SCA^{pos}KIT^{pos}CD45^{pos}EPCR^{pos}) as well as the E16.5 fetal liver (FL) (LIN^{neg}CD48^{neg}SCA^{pos}KIT^{pos}CD150^{pos}) (Fig. 7d). To functionally validate and evaluate the phenotypic Runx1Δ6 FL LT HSCs we performed transplantation experiments (Fig. 7e). Equal numbers of FACS-sorted E14 FLLT HSCs were transplanted (150 LT HSCs per mouse. Figure 7e) into sublethally irradiated mice. Both WT and Runx1 Δ 6 FL LT HSCs were able to reconstitute hematopoiesis in recipient mice; however, Runx1\Delta 6 LT HSCs exhibited signs of reduced capacity and/or fitness as the contribution to peripheral blood at 11 weeks was slightly lower (P < 0.05) (Fig. 7e). Although not statistically significant a similar trend was observed when analyzing week 12 donor contribution in the total bone marrow of the recipient mice, the bone-marrow lineage negative population (Ter119^{neg}CD3^{neg}B220^{neg}GR1^{neg}MAC1^{neg}) and the bone-marrowLSK (Ter119^{neg}CD3^{neg}B220^{neg}GR1^{neg}MAC1^{neg}SCA1^{pos}KIT^{pos}) population (Fig. 7f). Lineage commitment appeared unaffected, with

Fig. 7 | Loss of exon 6 containing Runx1 isoforms impacts HSC emergence.

a, Venn diagram showing the intersect between isoform-based entropy and dIF level differences between HEAGM and one or both extra-embryonic HE populations as well genes found to upregulated in the HEAGM (as shown in Fig. 6a) (left). Gene Ontology analyses across Wikipathways 2024 Mouse, KEGG 2021 human and MSigDB Hallmark 2020 databases (right). The input gene lists consisted of the 1,579 genes that showed differential isoform expression (entropy and/ or dIF) between HEAGM and one or both YS HE. Gene lists can be interrogated in Supplementary Table 4. Adjusted P values were calculated using Fisher's exact test with Benjamini-Hochberg correction **b**, Venn diagram depicting the intersects between genes upregulated in the HEAGM (as depicted in Fig. 6a), the shared HE profile (as depicted in Fig. 5a) and the 210 gene list of transcription and chromatin factors with distinct HEAGM isoform expression profiles (left). Cell identity analysis performed on all transcription and chromatin factors present in the list of genes with potential HE^{HSC}-selective isoform expression (middle). Adjusted P values were calculated using Fisher's exact test with Benjamini-Hochberg correction. Venn diagram intersect for the stemness genes identified in the cell identity analyses (right). The diagram shows if the genes were selected based on changes in Entropy or dIF. c, Emerging hematopoietic cells (CD31^{pos}KIT^{pos}CD45^{pos}) in E11.5 WT and CRISPR-Cas9 Runx1 ∆ exon 6 embryos identified by flow cytometry (Extended Data Fig. 1d). Percentage of emerging hematopoietic cells in E11.5 AGM regions (top). Each point represents a single AGM. Percentage of emerging hematopoietic cells in E11.5 YSs (bottom). Each point represents a single YS. WT n = 11, $\Delta \exp 6 n = 7$. Bars represent the average percentage of emerging hematopoietic cells ± s.e.m. Statistical test used was

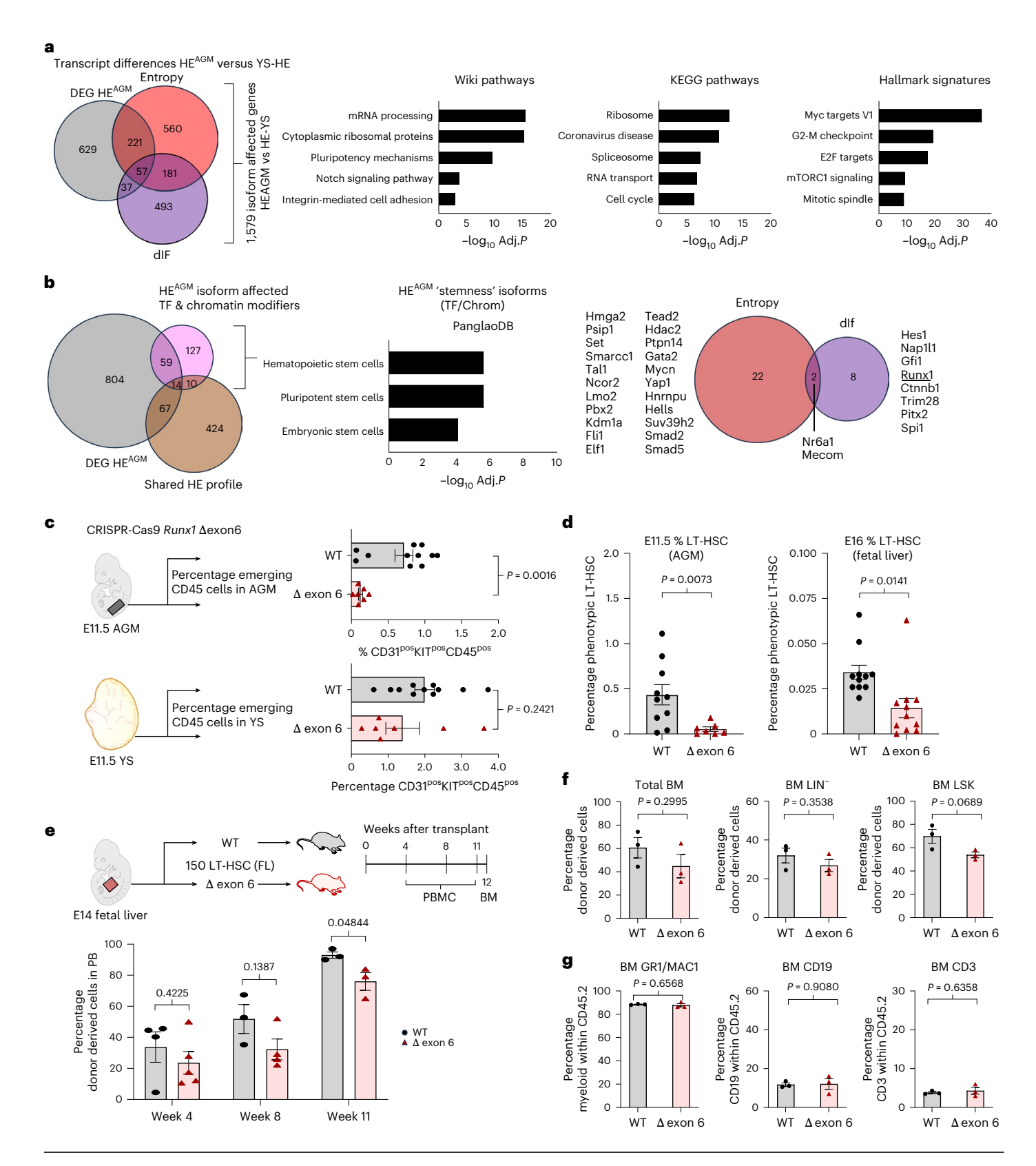
an unpaired two-tailed t-test. **d**, Phenotypic LT HSCs in E11.5 AGM and E16 FL identified by flow cytometry (Extended Data Fig. 1d), Left, percentage of LT HSCs in E11.5 AGMs. Each point represents a single AGM (WT n = 10, $\Delta \exp 6 n = 7$). Right, percentage of LT HSCs in E16 FLs. Each point represents a single FL (WT n = 11, $\Delta \exp 6 n = 11$). Bars represent the average percentage of LT $HSC \pm s.e.m.$ Statistical test used was an unpaired two-tailed t-test. **e**, Schematic of E14 FL LT HSCs transplantation experiments (top). A total of 150 phenotypic FLLT HSCs (CD45.2) were transplanted into sublethally irradiated NSGS mice (CD45.1). Donor contribution was followed for 12 weeks. Peripheral blood was analyzed by flow cytometry 4, 8 and 11 weeks post-transplant. At 12 weeks posttransplant the bone marrow (BM) was collected and analyzed by flow cytometry. Contribution of donor cells (CD45.2) to the peripheral blood of the transplanted mice at week 4 (WT n = 4, $\Delta \exp 6 n = 5$), 8 (WT n = 3, $\Delta \exp 6 n = 4$) and week 11 $(WT n = 3, \Delta exon 6 n = 3)$ (bottom). Bars represent the average percentage of donor derived blood cells \pm s.e.m. Unpaired two-tailed t-test. \mathbf{f} , Bar graphs presenting the percentage of donor derived cells in the BM of recipient mice 12 weeks post-transplant. Donor cell contribution to the total BM (left). Donor cell contribution to the lineage negative (TER-119^{neg}CD3^{neg}B220^{neg}GR1^{neg}MAC1^{neg}) BM population (middle). Donor cell contribution to the BM LSK (TER-119^{neg}CD3^{neg} B220^{neg}GR1^{neg}MAC1^{neg}SCA1^{pos}KITt^{pos}) population (right). n = 3. Bars represent the average percentage of donor derived blood cells ± s.e.m. Unpaired two-tailed t-test. g, Myeloid (GR1^{pos} and/or MAC1^{pos}), B cell (CD19^{pos}) and T cell (CD3^{pos}) lineage output of donor cells in recipient BM 12 weeks post-transplant. n = 3. Bars represent the average percentage of lineage contribution of donor derived blood cells \pm s.e.m. Unpaired two-tailed t-test.

the WT and Runx1 Δ 6 transplants showing comparable contributions to myeloid (GR1^{pos} and/or MAC1^{pos}), CD19^{pos} (B cell) and CD3^{pos} (T cell) populations (Fig. 7g).

Overall, these data indicate that loss of exon 6-containing Runx1 transcripts negatively affects early HSC emergence in the embryo and suggest a balance between exon 6 containing and exon 6 skipping *Runx1* transcripts is required for HSC emergence in the AGM.

Discussion

Hematopoietic cell therapies are potent treatment modalities for many blood diseases, including cancer. A major bottleneck for these treatments is sourcing sufficient patient compatible blood cells. Consequently, unraveling the molecular cues driving the generation of specific blood cell types, to reproduce these processes in vitro, is of great interest. HSCs and lineage-restricted EMP/LMPs are first established



from HE cells during embryogenesis. Intra-embryonic (dorsal aorta) HE, with HSC potential, has been the focus of multiple scRNA-seq studies. Single-cell transcriptomics of HE in the YS, the initial site of EMP and LMP generation, has so far garnered much less attention. Here we present a comprehensive full-length scRNA-seq dataset that covers three parallel embryonic EHT trajectories, each of which contains their own distinct HE population, skewed toward, respectively, HSPCs (intra-embryonic HE $^{\rm AGM}$), LMPs (YS HE $^{\rm YSA}$) and EMPs (YS HE $^{\rm YSP}$).

In contrast to the exclusively arterial identity of intra-embryonic HE^{27,49}, extra-embryonic HE activity^{50–52,32} has been reported throughout the YS endothelium, with an arterial identity being linked to LMP generation^{32,50,53}. Combining functional assays, whole-mount imaging and scRNA-seq, we reveal the presence of two different YS HE populations with divergent trajectories, one with an arterial endothelial identity and localization (HE^{YSA}) and another with a plexus endothelial identity and localization (HE^{YSA}). In line with the sequential emergence of embryonic EMPs and LMPs¹, the two YS HE populations also arise sequentially. Recently, EHT events within the large intra-and extra-embryonic arteries have been linked to the generation of short-term fetal-restricted HSPCs⁵⁴. The ability to enrich HE^{LMP}, using our newly identified CD24-LYVE1-MCAM antibody panel, warrants further characterization of the potential of this HE population.

Comparative analysis of all three EHT trajectories identified a shared HE signature composed of a small set of eight genes that can ascertain cells with HE characteristics regardless of their site of origin. Notably, transcriptional repressor Gfi1 and transcriptional activator Mycn were the only two transcription factors with HE-selective expression patterns. Gfi1 is an established player in EHT initiation via its ability to downregulate the endothelial program^{20,21} as also reflected in our data. Conversely, many genes that were newly activated (upregulated versus endothelium) within the HE populations were MYC target genes. It has been recently shown that, within the context of the AGM, Mycn expression is required for efficient EHT55. Our data suggest that Mycn, like Gfi1, is a HE-specific core functional component of EHT progression independent of the embryonic localization. Overall, many genes previously only reported/characterized in the context of AGM EHT, and suggested to be associated with the acquisition of HSPC potential, are also part of our universal HE profile, highlighting the need for comparative analyses to identify specific cell fate regulators.

Probing differential gene expression between HE populations revealed a high degree of similarity between YS HEYSA and intra-embryonic HEAGM, likely reflecting their shared arterial endothelial identity. In contrast, YS HE^{YSP} showed a distinct transcriptional profile, characterized by prominent expression of myeloid/hematopoietic genes, which was also partially observed in non-HE endothelial cells of the YS plexus. In HE^{AGM}, we found a prominent enrichment of genes involved in chromatin modification and RNA processing. The latter is especially interesting as several recent studies have indicated that changes in the isoform landscape play a role in the emergence of the hematopoietic system and HSC biology^{40,56}. One study by Wang et al. focusing on EHT in the AGM has shown distinct changes in isoform expression profiles in the transition toward HE and subsequently T1-preHSCs⁴⁰. The affected genes were involved in RNA metabolic processes, including RNA splicing, RNA transport and ribonucleoprotein complex biogenesis⁴⁰. Our findings are consistent with these observations and further highlight this phenomenon as specific to HE^{AGM}. In contrast, differences in the isoform landscapes between the two YS HE populations were minimal, suggesting that their identity and potential are predominantly driven by differential gene expression. Notably, we observed HEAGM specific changes in isoform expression patterns for transcription/chromatin factors, including Runx1, associated with a stem cell identity. We experimentally demonstrated here that limiting the isoform diversity of Runx1, by introducing an in-frame deletion of exon 6 in all transcripts, negatively impacted immunophenotypic LT HSC detection in AGM and FL. Of note, the absence of $\Delta 6$ transcripts has previously been shown to negatively impact HSPCs, including LT HSCs, in the bone marrow of adult mice⁴⁷. Indeed, it has been reported that Runx1 Δ 6 isoforms can enhance the transactivation ability of the exon 6 containing Runx1 isoforms in vitro⁴⁷. More recently, the interaction between the ETS factor ELF1 and RUNX1 has been shown to enhance HSC self-renewal and prevent HSC differentiation⁵⁷. Notably, the RUNX1 E26 transformation-specific (ETS) factor binding domain has been localized to the region encompassing *Runx1* exon 6 and exon 7 (ref. 58). Together, these data point toward a role for balanced expression of Runx1 exon 6 and Runx1 Δ exon 6 transcripts in lineage choice.

The dataset presented here provides a unique resource for further characterization of the three HE populations in the mouse embryo. A particularly intriguing observation is that HE^{AGM} exhibits a distinct isoform landscape compared to the YS HE populations; however, identifying isoform combinations that directly determine cell fate remains a substantial challenge. This not only due to the underlying biology, such as the higher isoform entropy observed in HE^{AGM}, but also due to technical limitations in isoform resolution from short-read Smart-seq2 data. To attempt to address this, we performed long-read nanopore sequencing on a subset of 220 (160 HE and 60 early progenitors) cells from our Smart-seq2 dataset. While this approach confirmed a global shift toward higher isoform entropy in HE^{AGM} (Extended Data Fig. 7g), the coverage achieved was lower than that of the Smart-seq2 data and insufficient for robust isoform-level analysis. Further advancements in the sequencing depth and accuracy of long-read single-cell technologies will be particularly beneficial for isoform quantification, transcript coverage and the discovery of novel isoforms. Another limitation of our study is the difficulty in reliably predicting the fate of individual transient HE cells at the single-cell level. For example. within the HE^{AGM} population, we cannot tell which cells will become HSC versus other progenitors. Likewise, in HEYSP and HEYSA populations, we cannot predict erythroid versus myeloid or lymphoid versus myeloid outcomes. Current transcriptomic comparisons using predefined signatures (HSCs, EMPs and LMPs) lack the resolution to detect lineage commitment this early in hematopoietic emergence²⁶. These early transient cell states, which may disappear before cells become committed progeny, likely influence fate decisions. This underscores the need to compare HE populations with different developmental outcomes, not just committed populations. As discussed above, many 'AGM-specific' EHT genes associated with HSPC potential are expressed in multiple HE subsets, indicating a role in EHT rather than in lineage commitment. Identifying and validating these transient states will require improved perturbation screens, lineage tracing, and novel analytical approaches.

To conclude, our results reveal three distinct EHT trajectories and suggest that hematopoietic fate decisions in HE^{AGM}, including those toward an HSC cell fate, could at least in part be governed on an isoform level. Overall, our scRNA-seq dataset capturing three distinct EHT trajectories, giving rise to EMPs, LMPs and HSPCs, represents a powerful and unique resource for future investigations of cell fate decision in different HE.

Methods

Mouse embryo generation and processing

Mouse work was performed in accordance with the United Kingdom Animal Scientific Procedures Act (ASPA) 1986. Animal experiments performed at the Cancer Research United Kingdom Manchester Institute (CRUK-MI) were approved by the Animal Welfare and Ethics Review Body of the CRUK-MI. Experiments performed at the University of Oxford were approved by the Oxford Clinical Medicine Ethical Review Committee. Mice were housed in individually ventilated cages under standard conditions, including a 12-h light–dark cycle, ambient temperature of 19–23 °C and relative humidity of 45–65%, in accordance with UK Home Office guidelines and institutional protocols. The transgenic reporter mouse lines (strain C57BL/6JOlaHsd) *Gfi1* (refs. 20,26,29)

and *Runx1b*^{RFP} (refs. 26,28) and *Vwf*^{eGFP} (ref. 31) have been described previously. Vaginal plug detection was considered as E0.5 and staging was confirmed for each embryo at the time of collection by visual inspection. For experiments using the *Gfi1*^{GFP} and *Runx1b*^{RFP} reporters, WT Hsd:ICR (CD-1) females were used to set up breeding pairs ensuring reporter sorted cells were exclusively obtained from embryos. The following primers (custom DNA Oligos Merck) were used to genotype embryos. Gfi1GFP, forward1_5'-CCCTTCTCAGAACTCAGAG-3', forward2_5'-GGAAACGAGGTGGCTTGGAG-3', reverse_5'-GTCTTGT AGTTGCCGTCGTC-3' (WT: 245 bp, Kl:390 bp). Runx1bRFP, forward1_5'-ATGGTGATACAAGGGACATCTTCCC-3', forward2_5'-ACTTGTAT GTTGGTCTCCCG-3', reverse_5'-ACCAGAGACTTCTACTACAGGC-3' (WT, 550 bp; Kl, 200 bp).

For the single cell RNA-seq and in vitro functional assays, dissected YSs were digested in a mix of Collagenase IV (2 mg ml⁻¹, Worthington) and DNase I (200 U ml⁻¹, Calbiochem) at 37 °C for 15 min. The dissociated cells were pelleted (300g for 5 min at 4 °C) and resuspended in phosphate buffered saline (PBS) containing 10% fetal bovine serum (FBS) and further processed for FACS analyses/sorting.

For YS preparation for whole-mount immunofluorescence staining 25,59,60 , embryos were dissected in calcium and magnesium-free PBS, 10% FBS and 0.1 mM EDTA. Embryos were fixed in PBS 4% paraformaldehyde for 1 h, rinsed with PBS ($3\times$, 5 min at RT) and incubated in 50% methanol in PBS (4 °C for 10 min). Samples were stored at -20 °C in 100% methanol until further use.

CRISPR-Cas9 Runx1 \(\Delta \) exon 6 embryos

One-cell-stage embryos were electroporated with guides targeting the exon 6 of the *Runx1* gene and Cas9 protein, then reimplanted into surrogate mothers⁴⁸. The guides targeted the following sequences flanking exon 6 of *Runx1* (PAM sequences are underscored) (custom DNA Oligos Merck): 5′-CCTCCCGGTCCCTACACTAGGAC-3′ and 5′-CCCACGAGCCCACTACCCTG-3′ At E11.5, embryos were collected and genotyped using primer pairs flanking exon 6: forward1_5′-AGTGGGCTGAAGGAACCT-3′, reverse1_5′-ACGGATTACAGTCTCCA GGA -3′ (WT 779 bp, ko 539 bp) and forward2_5′ CAAGGGGCAATGTCCAACAA -3′, reverse2_5′- ACCTGGAACCGATAACTGCA -3′ (WT 637 bp, ko 397 bp). The AGMs of these embryos were subsequently dissected and processed and analyzed by flow cytometry to identify any defects in blood cell development²⁶. For E16.5 FLs, dissected livers were crushed with the end of a 1-ml syringe through a 40-μm cell strainer into IMDM + 10% FBS.

Transplantation assay of Runx1 Δ exon 6 embryos

Female NSGS (NOD.Cg-Prkdcscid Il2rgtm1Wjl Tg(CMV-IL3,CSF2, KITLG)1Eav/MloySzJ) (CD45.1) mice, aged 8–12 weeks, were used as recipients after two rounds of irradiation at 200 cGy, 3 h apart. Runx1 Δ exon 6 heterozygote males and females (CD45.2) between the ages of 2–6 months were mated, and vaginal plug detection was considered as day 0.5. E14.5 FLs were genotyped and processed for FACS isolation of LT HSCs (TER-119^negCD3^negB220^negGR1^negCD48^negSCA1^posKIT^posCD150^pos) as described above (Supplementary Table 5 lists the antibodies used). Each recipient received 150 LT HSCs intravenously in 200 μ l of PBS, along with 20,000 nucleated bone- marrow cells from NSGS donors as a support. Peripheral blood was taken in weeks 4, 8 and 11 after transplantation and terminal samples were collected in week 12.

Flow cytometry

Flow cytometry analyses were performed on a BD LSRFortessa X-20 Cell Analyzer (BD Biosciences) and a Novocyte Quanteon (Agilent). All cell sorting was performed on a BD FACSAria III Cell Sorter (BD Biosciences). Antibodies used for FACS are listed in Supplementary Table 5. For scRNA-seq cells were directly sorted into lysis buffer and snap-frozen before further processing. FlowJo software (BD Biosciences) was used to analyze all FACS data.

In vitro single-cell assays

All single cell assays on YS-derived cells were performed using co-culture with OP9 stromal cells (mouse bone-marrow stromal cell line; ATCC CRL-2749 obtained from the American Type Culture Collection) In brief, hematopoietic activity assays were performed by FACS sorting single YS cells onto OP9 cells in 96-well plates (one cell per well). The cells were cultured in IMDM (Invitrogen), 10% fetal calf serum, L-glutamine (4 mM), penicillin–streptomycin (50 U ml $^{-1}$), α -monothioglycerol (15 mM), ascorbic acid (50 ng ml $^{-1}$), transferrin (180 μ g ml $^{-1}$), IL-11 (5 ng ml $^{-1}$), EPO (2 U ml $^{-1}$), oncostatin M (10 ng ml $^{-1}$), IL-6 (20 ng ml $^{-1}$), bFGF (10 ng ml $^{-1}$), IL-3 (100 ng ml $^{-1}$), SCF (100 ng ml $^{-1}$), Flt3L (100 ng ml $^{-1}$) and 2% leukemia inhibitory factor (LIF) supernatant for 10 days before microscopically scoring wells that showed signs of hematopoietic proliferation.

Hematopoietic lineage potential assays were performed similarly but with a different media composition: αMEM (Invitrogen), 10% fetal calf serum, L-glutamine (4 mM), penicillin–streptomycin (50 U ml $^{-1}$), 2-mercaptoethanol (100 mM), SCF (5 ng ml $^{-1}$), IL-7 (2 ng ml $^{-1}$) and Flt3L (5 ng ml $^{-1}$). After 7 days, wells containing proliferating cells were passaged onto fresh OP9 cells and culture for 7 additional days. Lineages of the hematopoietic cells were defined based on FACS analyses of CD19, CD11b and TER119 cell surface expression (Supplementary Table 5).

Hematopoietic colony-forming unit assays

FACS-sorted YS and FL populations were examined by culturing cells, with (YS) or without (YS and FL) previous co-culture on OP9 for 48 h, in a semi-solid methylcellulose matrix (MethoCult GF M3434, Stem Cell Technologies). Colony output was determined after 7–10 days of culture by colony morphology. Where applicable, OP9 co-culture was performed in IMDM (Invitrogen), 10% fetal calf serum, L-glutamine (4 mM), penicillin–streptomycin (50 U ml $^{-1}$), α -monothioglycerol (15 mM), ascorbic acid (50 ng ml $^{-1}$), transferrin (180 μ g ml $^{-1}$), IL-11 (5 ng ml $^{-1}$), EPO (2 U ml $^{-1}$), oncostatin M (10 ng ml $^{-1}$), IL-6 (20 ng ml $^{-1}$), bFGF (10 ng ml $^{-1}$), IL-3 (100 ng ml $^{-1}$), SCF (100 ng ml $^{-1}$), Flt3L (100 ng ml $^{-1}$) and 2% LIF supernatant.

Whole-mount Immunofluorescence staining and analyses

Whole-mount staining and analyses^{25,59,60}. All primary and secondary antibodies used for immunofluorescence are listed in Supplementary Table 5. Fixed (4% paraformaldehyde) samples were routinely stored at -20 °C in 100% methanol (see 'mouse embryo generation and processing' section). Following rehydration, YS samples were treated with a permeabilizing blocking solution (0.2% Triton X-100, 2% donkey serum and 2% FBS) and incubated overnight with primary antibodies. The next day a second step with secondary antibodies was carried out. After staining, YSs were cleared overnight in a 50% solution of glycerol in PBS at 4 °C and then flat-mounted on Superfrost glass slides. Samples were imaged using a Zeiss 710 confocal microscope equipped with a LD LCI Plan-Apochromat ×25/0.8 Imm Corr DIC M27 objective or an EC Plan-Neofluar ×40/1.30 Oil DIC M27 objective. Confocal image acquisition was carried out using Zeiss Zen software v.2.3 SP1; image processing and analysis was carried out using IMARIS Viewer software v.9.7.2 (Bitplane), Imagel/Fiji (v.2.3.5-2.9.0) and Adobe Photoshop CC 2021. vWF-associated and Lyve1-associated mean of fluorescence intensity (MFI) was measured by ImageJ/Fiji as mean of gray value in a selected area (an example is shown in Fig. 3a) and expressed in arbitrary units. The ratio of vWF-associated MFI to Lyve1-associated MFI was calculated for the same area. Cell counts were performed using Fiji/ImageJ Cell Counter tool.

scRNA-seq and data processing

Single cells were sorted into wells of a 384-well plate containing lysis buffer and snap-frozen. Libraries were prepared using a modified Smart-seq2 protocol⁶¹. Paired-end 38 bp or 75 bp sequencing was carried out on the NextSeq500 or NovaSeq 6000 platform (Illumina).

Following sequencing, the raw fastq files were obtained by bcltoFastq conversion (v.2.20.0.422) and were subsequently aligned to the mm10 reference genome using STAR aligner (v.2.7.9a) with the argument 'STARsolo'. This argument allowed simultaneous mapping of reads and quantification of gene expression. The reference genome and gene transfer format file were downloaded from 10x Genomics webpage at https://cf.10xgenomics.com/supp/cell-exp/refdata-gex-mm10-2020-A. tar.gz. The output of 'STARsolo' was loaded into R (v.4.1.0) using the Bioconducter package DropletUtils (v.1.12.1). Downstream analyses were conducted in R using SingleCellExperiment (v.1.14.1) and Seurat (v.4.0.6). A total of 2,365 cells was sequenced (795 on the NextSeq500 and 1570 on the NovaSeq 6000). Next, cells with <2,000 detected genes, >15% mitochondrial content and >10% hemoglobin percentage were excluded, leaving 2,255 high quality cells (705 on the NextSeq500 and 1,550 on the NovaSeq 6000). This filtering process was adopted as previously described26.

Analysis of YS EHT scRNA-seq datasets

A total of 1,469 scRNA-seq cells were considered high quality YS cells (115 on the NextSeq5000 and 1,354 on the NovaSeq). During the sequencing, 225 technical replicates (the same cells sequenced twice) were introduced. Duplicated technical replicates were removed, retaining cells with that yielded the highest number of genes leaving a total of 1,214 YS cells. Following read quantification and filtering, single cell analysis was performed using the scater (v.1.20.1) package. Raw counts were log-normalized (logNormCounts), gene variance was modeled (modelGeneVar) and the top 2,000 highly variable genes (HVGs) were identified (getTopHVGs). Following normalization, cells were subsequently clustered using graph-based clustering (buildSNNGraph, parameters: k = 10, use.dimred = 'PCA'). Based on graph-based clustering, we noted groups of outlier cells that (1) contained high percentage of ribosomal genes with the lowest genes detected; (2) contained high expression of hemoglobin gene (Hbb-y); (3) were potential mesenchymal cells with high expression of mesenchymal genes (Dlk1 and Ptn); (4) were a distinct cluster of cells expressing the marker *Folr1*; and (5) were matured megakaryocyte or platelet-contaminating cells with high expression Pf4, Gp5 and Gp5. These outlier cells (n = 139) were excluded leaving 1,075 YS cells. We next used unsupervised hierarchical clustering (hclust) utilizing the 'ward.D2' distance measure to cluster the cells. The number of clusters were determined based on the dynamic tree cut functionally (cutreeDynamic) yielded six clusters.

Integration of AGM and YS EHT scRNA-seq datasets

AGM datasets were obtained from the Gene Expression Omnibus (GEO) (GSE150412)²⁶. From the raw fastq sequencing files, we used the same processing pipeline as was used in the YS EHT scRNA-seq (as described above) to obtain sequencing counts in the AGM dataset. The raw counts of the AGM and the raw counts of YS data were jointly analyzed as a single AnnData object using the scanpy workflow (v.1.6.1). Low-quality cells were removed as previously described²⁶ and using the same criteria described above. As the previous AGM scRNA-seq cells were sequenced on the NextSeq500 platform and the YS scRNA-seq cells were sequenced on the NovaSeq, a number of AGM FACS-ENDO (n = 21) were concurrently isolated, processed and sequenced on the NovaSeq platform with the YS FACS population. Two strategies were employed to determine and subsequently mitigate batch effects. First, differential expression was performed between the FACS-ENDO populations sequenced across the two platforms. Genes with greater than log₂FC of 1.5 and adjusted *P* value < 0.01 were considered as genes associated with experimental batches. Second, gene that showed variation in detection rates (>50%) between the sequencing platform were identified. These genes were excluded from further analysis.

To focus on the similarity and differences during EHT in the AGM and YS, the non-EHT related populations (AGM venous endothelial and AGM mesenchymal) and the YS FACS-HE $^{\rm KIT-Neg}$ cells, YS clusters that

have progressed beyond the early progenitor stage (YS EMP and YS LMP) were computationally excluded. The raw counts of the remaining cells were log-normalized (sc.pp.normalize total) and HVGs identified (sc.pp.highly variable genes). To generate low dimensional representation, principal-component analysis (PCA) (sc.tl.pca) was conducted on the scaled expression values (sc.pp.scale). The top 50 principal components were used to determine a k-nearest neighbor graph (sc.pp.neighbors(n neighbors = 20)). Two rounds of semi-supervised Leiden clustering were carried out to identify clusters. Initially, an unsupervised Leiden clustering (sc.tl.leiden(resolution = 2)) was used followed by a semi-supervised merging of clusters with <40 cells. Next, to generate a simplified graph representation of the data, partition-based graph abstraction (PAGA) (sc.pl.paga) was used based on the Leiden groupings. The final UMAP representation was generated using PAGA-initialized positions. The scanpy results were imported into R, where the final representations of the data were generated.

Differential expression analysis and construction of a common HE signature

Differential expression between two groups was performed using the 'limma' package (v.3.54.2) and the 'voom' function. Before differential expression, genes with more than 90% dropout were excluded. Additionally, to mitigate skewing of differential gene expression analyses between HE groups in the HE^{AGM}, HE^{YSA} and HE^{YSP} trajectories, HE clusters were downsampled to the cluster with the lowest cell number in each individual HE. This resulted in three normalized HE populations, each encompassing two clusters with equal representation. The normalized HE was used to generate a universal HE gene expression profile by performing differential expression analyses versus the closest endothelial population and versus the most progressed hematopoietic cells in our dataset (EMPs and LMPs) as illustrated in Extended Data Fig. 3a. Only genes expressed in at least 33% of the cells (for each type of HE) that displayed a log₂FC > 1 and false discovery rate (FDR) < 0.05 versus either the endothelial or hematopoietic ends of the trajectory were taken forward. For inter-HE differential gene expression, the following cut-offs were used: $log_2FC > 1.5$, FDR < 0.05 and percent of gene-expressing cells (in the upregulated population) >50%. Differentially expressed gene lists were interrogated for enrichment of biological features using the online Enrichr tool⁶². Only results with an adjusted Pvalue < 0.05, an odds ratio > 2 and > 5 gene hits were taken forward.

Calculation of gene signature scores

To determine a collective gene signature enrichment, the UCell package 63 (v.2.2.0) was used. Based on a given gene list, the UCell signature score (ScoreSignatures_UCell) was calculated for each cell. Gene list for the different signatures used are listed in Supplementary Table 1. EMP-fate and LMP-fate signature were constructed by intersecting the DEGs between EMPs and LMPs (adjusted P value < 0.05) and YS clusters p1 and p2 (adjusted P value < 0.05).

Statistical comparison of UCell scores. To compare UCell signature enrichment between cell clusters, pairwise statistical comparisons were performed using the Wilcoxon rank-sum test (Mann–Whitney U-test). This nonparametric test was chosen due to the non-normal distribution of UCell scores, which typically exhibit right-skewed distributions with a high proportion of zero values. Statistical significance was assessed at P = 0.05, and comparisons were visualized using the ggsignif package. For analyses involving multiple comparisons, P values were adjusted using the Benjamini–Hochberg method to control the FDR.

Analysis of publicly available scRNA-seq data. We analyzed the published scRNA-seq data of Fadlullah et al.²⁶, Zhu et al.³⁰, Hou et al.³⁶, Wang et al.³⁸ and Li et al.³⁷. In the scRNA-seq data from Fadlullah et al.²⁶, we reprocessed the data from raw fastq files using the STAR-solo workflow described above. We extracted cluster information

and retained the following AGM EHT population: Arterial endothelial, Pre-HE, HE-HSC, and IAHC. In the scRNA-seq data from Zhu et al. 30, we directly downloaded the count matrix files and the cell annotations from GEO (GSE137116). The Zhu et al. data were filtered to retain cells from E10.5 embryos. Furthermore, only cells from the populations related to EHT were kept: 'Endo (other)', 'Endo (Wnt_low) [AE]', 'Endo (Wnt_high) [AE]', 'Conflux endo [AE]', 'Pre-HE [AE]', 'HE' and 'IAC'. In the scRNA-seq data from Hou et al. (GSE139389), we downloaded the count matrix files from GEO and extracted cluster annotations from the supplementary data (sheet 8, 41422 2020 300 MOESM5 ESM. xls). We retained AGM E10.0-E10.5 endothelial cells corresponding to the following populations: 'vECs' (venous endothelial cells), 'earlyAEC' (early arterial endothelial cells), 'lateAEC' (late arterial endothelial cells), 'Neurl3-EGFP'' (Neurl3-positive cells), 'tif-HEC' (transcriptomic and immunophenotypic and functional HEC) and 'HC' (hematopoietic cells). In the scRNA-seq data from Wang et al. (GSE167588), we downloaded count matrix files from GEO and extracted cluster annotations from the supplementary data (11427_2021_1935_MOESM7_ESM.xls). The dataset included both YS and caudal region populations. We retained the YS: 'YS_ApInr+EC' (YS ApInr-positive endothelial cells), 'YS_aEC' (YS arterial endothelial cells), 'YS_HE' (YS HE), 'YS_Ery' (YS erythroid cells). In the scRNA-seq data from Li et al. (GSE173833), we downloaded count matrix files from GEO (GSM5281418) for YS PK44 (CD41⁻CD43⁻CD45 CD31+CD201+Kit+CD44+) cells from E10.0 embryos. As cluster annotations were not provided, we performed hierarchical clustering using DEGs between endothelial-biased and hematopoietic-biased populations as described in the original publication (Supplementary Table 1 of the publication). We used Ward's linkage method with Euclidean distance and dynamic tree cutting to identify three distinct clusters (PK44-endo, PK44-mix and PK44-hematopoetic) representing different stages of YS cell progression.

Publicly available GFI genomic binding data

The following three GFI binding datasets (GEO accession codes: GSE57251, GSE22178, GSE69101) obtained from early hematopoietic populations were used: (1) GFI1 and GFI1b binding data from DamID of HE from embryonic stem cells, GEO_GSE57251: GSM1377856, GSM1377857 and GSM1377858 (ref. 21); (2) GFI1b binding data from ChIP-seq of HPC7 cell line (downloaded from Supplementary Table 1 of the online version of the manuscript). Also available at GEO GSE22178: GSM552235 and GSM552236 (ref. 35); (3) GFI1 and GFI1b binding data from ChIP-seq of mES-derived early hematopoietic progenitors, GEO GSE69101: GSM1692809, GSM1692853 and GSM1692854 (ref. 34). In each of the studies mentioned, the BED files were downloaded and were annotated with ChIPpeakAnno (v.3.20.1). Peaks were filtered to retain regions within 3 kb of transcription start site for ChIP-seq data and 5 kb of the gene body for DamID data. Genes were identified as potential GFI targets if binding was observed in at least one GFI1 and one GFI1b dataset.

Single-cell isoform transcript analyses

SMARTseq. Raw reads were aligned and quantified with Salmon⁶⁴ (v.1.10.2; --libtype OU) against GENCODE transcripts (release 37). Quantification files were read into R using either tximport (v.1.28.0) or importIsoformExpression (IsoformSwitchAnalyzeR v.2.0.1)^{42,65}. Isoform switching analysis was perfomed using IsoformSwitchAnalyzeR with isoformSwitchTestSatuRn⁴²; significant isoform switches were defined as those with an adjusted $P \le 0.05$ and |dIF| > 0.1. Splicing entropy was assessed using SplicingFactory (v.1.8.0)⁴¹; significant entropy changes were defined with adjusted $P \le 0.05$. To detect a skew in entropy changes a chi-squared goodness of fit test was applied.

Nanopore sequencing. Data were basecalled using Dorado (v.0.9.1) (Oxford Nanopore Technologies Dorado, 2025; https://github.com/nanoporetech/dorado) using the high-accuracy model

(dna_r10.4.1_e8.2_400bps_hac@v5.0.0). Raw reads were trimmed for SMARTseq adapters using bbduk.sh (v.39.08)⁶⁶. Chimeric reads were filtered from the data using YACRD (v.1.0.0) and porechop (v.0.2.4)^{67,68}. Cleaned reads were aligned to GENCODE transcripts (release 37) using Minimap2 (v.2.26)⁶⁹, retaining a maximum of ten alignments per read. Alignments were quantified using NanoCount (v.1.0.0.post6)⁷⁰. Abundance files were read into R (v.4.3.0) filtered for low library size samples using findOutliers (scuttle v.1.10.3; type = 'lower', nmads = 1) and normalized using DESeq2 (v.1.40.2)⁷¹. Estimated and normalized counts were subject to analysis using IsoformSwitchAnalyzeR and Splicing-Factory as previously described 41,42.

Reporting summary

Further information on research design is available in the Nature Portfolio Reporting Summary linked to this article.

Data availability

Gene expression data can be queried at https://shiny.cruk.manchester. ac.uk/AGM_YS_dataset_final/. Raw data are deposited in the GEO under accession codes GSE274544 and GSE309071. Three Source data files accompany this manuscript (for the main figures, extended figures and tables).

Code availability

Code is available at https://github.com/zakiF/PublishedPapers/tree/master/YolkSac_AGM <u>and</u> https://github.com/RASellers-CRUK/GL IsoformAnalysis

References

- Dzierzak, E. & Bigas, A. Blood development: hematopoietic stem cell dependence and independence. Cell Stem Cell 22, 639–651 (2018).
- Neo, W. H., Lie-A-Ling, M., Fadlullah, M. Z. H. & Lacaud, G. Contributions of embryonic HSC-independent hematopoiesis to organogenesis and the adult hematopoietic system. Front. Cell Dev. Biol. 9, 631699 (2021).
- Bertrand, J. Y. et al. Three pathways to mature macrophages in the early mouse yolk sac. *Blood* 106, 3004–3011 (2005).
- Palis, J., Robertson, S., Kennedy, M., Wall, C. & Keller, G. Development of erythroid and myeloid progenitors in the yolk sac and embryo proper of the mouse. *Development* 126, 5073–5084 (1999).
- McGrath, K. E. et al. Distinct sources of hematopoietic progenitors emerge before hscs and provide functional blood cells in the mammalian embryo. Cell Rep. 11, 1892–1904 (2015).
- Boiers, C. et al. Lymphomyeloid contribution of an immune-restricted progenitor emerging prior to definitive hematopoietic stem cells. Cell Stem Cell 13, 535–548 (2013).
- Lin, Y., Yoder, M. C. & Yoshimoto, M. Lymphoid progenitor emergence in the murine embryo and yolk sac precedes stem cell detection. Stem Cells Dev. 23, 1168–1177 (2014).
- Medvinsky, A. & Dzierzak, E. Definitive hematopoiesis is autonomously initiated by the AGM region. Cell 86, 897–906 (1996).
- 9. Taoudi, S. et al. Extensive hematopoietic stem cell generation in the AGM region via maturation of VE-cadherin+CD45+ pre-definitive HSCs. *Cell Stem Cell* **3**, 99–108 (2008).
- 10. Kobayashi, M. et al. HSC-independent definitive hematopoiesis persists into adult life. *Cell Rep.* **42**, 112239 (2023).
- 11. Patel, S. H. et al. Lifelong multilineage contribution by embryonic-born blood progenitors. *Nature* **606**, 747–753 (2022).
- Boisset, J. C. et al. In vivo imaging of haematopoietic cells emerging from the mouse aortic endothelium. *Nature* 464, 116–120 (2010).
- Chen, M. J., Yokomizo, T., Zeigler, B. M., Dzierzak, E. & Speck, N. A. Runx1 is required for the endothelial to haematopoietic cell transition but not thereafter. *Nature* 457, 887–891 (2009).

- Jaffredo, T., Gautier, R., Eichmann, A. & Dieterlen-Lievre, F.
 Intraaortic hemopoietic cells are derived from endothelial cells during ontogeny. *Development* 125, 4575–4583 (1998).
- Lacaud, G. & Kouskoff, V. Hemangioblast, hemogenic endothelium, and primitive versus definitive hematopoiesis. Exp. Hematol. 49, 19–24 (2017).
- Lancrin, C. et al. The haemangioblast generates haematopoietic cells through a haemogenic endothelium stage. *Nature* 457, 892–895 (2009).
- 17. Lie-A-Ling, M. et al. Regulation of RUNX1 dosage is crucial for efficient blood formation from hemogenic endothelium. Development https://doi.org/10.1242/dev.149419 (2018).
- Okuda, T., van Deursen, J., Hiebert, S. W., Grosveld, G. & Downing, J. R. AML1, the target of multiple chromosomal translocations in human leukemia, is essential for normal fetal liver hematopoiesis. Cell 84, 321–330 (1996).
- Wang, Q. et al. Disruption of the Cbfa2 gene causes necrosis and hemorrhaging in the central nervous system and blocks definitive hematopoiesis. Proc. Natl Acad. Sci. USA 93, 3444–3449 (1996).
- Lancrin, C. et al. GFI1 and GFI1B control the loss of endothelial identity of hemogenic endothelium during hematopoietic commitment. *Blood* 120, 314–322 (2012).
- Thambyrajah, R. et al. GFI1 proteins orchestrate the emergence of haematopoietic stem cells through recruitment of LSD1. Nat. Cell Biol. 18, 21–32 (2016).
- 22. Hadland, B. K. et al. A requirement for Notch1 distinguishes 2 phases of definitive hematopoiesis during development. *Blood* **104**, 3097–3105 (2004).
- Thambyrajah, R. & Bigas, A. Notch signaling in HSC emergence: when, why and how. *Cells* https://doi.org/10.3390/cells11030358 (2022).
- Neo, W. H. et al. Cell-extrinsic hematopoietic impact of Ezh2 inactivation in fetal liver endothelial cells. *Blood* 131, 2223–2234 (2018).
- Neo, W. H. et al. Ezh2 is essential for the generation of functional yolk sac derived erythro-myeloid progenitors. *Nat. Commun.* 12, 7019 (2021).
- Fadlullah, M. Z. H. et al. Murine AGM single-cell profiling identifies a continuum of hemogenic endothelium differentiation marked by ACE. *Blood* 139, 343–356 (2022).
- Yokomizo, T. & Dzierzak, E. Three-dimensional cartography of hematopoietic clusters in the vasculature of whole mouse embryos. *Development* 137, 3651–3661 (2010).
- Sroczynska, P., Lancrin, C., Kouskoff, V. & Lacaud, G. The differential activities of Runx1 promoters define milestones during embryonic hematopoiesis. *Blood* 114, 5279–5289 (2009).
- Yucel, R., Kosan, C., Heyd, F. & Moroy, T. Gfi1:green fluorescent protein knock-in mutant reveals differential expression and autoregulation of the growth factor independence 1 (Gfi1) gene during lymphocyte development. J. Biol. Chem. 279, 40906–40917 (2004).
- 30. Zhu, Q. et al. Developmental trajectory of prehematopoietic stem cell formation from endothelium. *Blood* **136**, 845–856 (2020).
- 31. Sanjuan-Pla, A. et al. Platelet-biased stem cells reside at the apex of the haematopoietic stem-cell hierarchy. *Nature* **502**, 232–236 (2013).
- Yzaguirre, A. D. & Speck, N. A. Insights into blood cell formation from hemogenic endothelium in lesser-known anatomic sites. *Dev. Dyn.* 245, 1011–1028 (2016).
- 33. Thambyrajah, R. et al. HDAC1 and HDAC2 modulate TGF-β signaling during endothelial-to-hematopoietic transition. *Stem Cell Rep.* **10**, 1369–1383 (2018).
- Goode, D. K. et al. Dynamic gene regulatory networks drive hematopoietic specification and differentiation. *Dev. Cell* 36, 572–587 (2016).

- Wilson, N. K. et al. Combinatorial transcriptional control in blood stem/progenitor cells: genome-wide analysis of ten major transcriptional regulators. Cell Stem Cell 7, 532–544 (2010).
- 36. Hou, S. et al. Embryonic endothelial evolution towards first hematopoietic stem cells revealed by single-cell transcriptomic and functional analyses. *Cell Res* **30**, 376–392 (2020).
- 37. Li, Y. Q. et al. Spatiotemporal and functional heterogeneity of hematopoietic stem cell-competent hemogenic endothelial cells in mouse embryos. *Front. Cell Dev. Biol.* **9**, 699263 (2021).
- 38. Wang, C. et al. Adult-repopulating lymphoid potential of yolk sac blood vessels is not confined to arterial endothelial cells. *Sci. China Life Sci.* **64**, 2073–2087 (2021).
- 39. Thambyrajah, R. et al. Cis inhibition of NOTCH1 through JAGGED1 sustains embryonic hematopoietic stem cell fate. *Nat. Commun.* **15**, 1604 (2024).
- 40. Wang, F. et al. Single-cell architecture and functional requirement of alternative splicing during hematopoietic stem cell formation. *Sci. Adv.* **8**, eabg5369 (2022).
- 41. Danko, B., Szikora, P., Por, T., Szeifert, A. & Sebestyen, E. SplicingFactory-splicing diversity analysis for transcriptome data. *Bioinformatics* **38**, 384–390 (2022).
- Vitting-Seerup, K. & Sandelin, A. IsoformSwitchAnalyzeR: analysis
 of changes in genome-wide patterns of alternative splicing and
 its functional consequences. *Bioinformatics* 35, 4469–4471
 (2019)
- 43. Lv, J. et al. Endothelial-specific m(6)A modulates mouse hematopoietic stem and progenitor cell development via Notch signaling. *Cell Res.* **28**, 249–252 (2018).
- 44. Zheng, J. et al. Profilin 1 is essential for retention and metabolism of mouse hematopoietic stem cells in bone marrow. *Blood* **123**, 992–1001 (2014).
- 45. Draper, J. E. et al. RUNX1B expression is highly heterogeneous and distinguishes megakaryocytic and erythroid lineage fate in adult mouse hematopoiesis. *PLoS Genet.* **12**, e1005814 (2016).
- Draper, J. E. et al. Mouse RUNX1C regulates premegakaryocytic/ erythroid output and maintains survival of megakaryocyte progenitors. *Blood* 130, 271–284 (2017).
- Komeno, Y. et al. Runx1 exon 6-related alternative splicing isoforms differentially regulate hematopoiesis in mice. *Blood* 123, 3760–3769 (2014).
- 48. Modzelewski, A. J. et al. Efficient mouse genome engineering by CRISPR-EZ technology. *Nat. Protoc.* **13**, 1253–1274 (2018).
- de Bruijn, M. F., Speck, N. A., Peeters, M. C. & Dzierzak, E. Definitive hematopoietic stem cells first develop within the major arterial regions of the mouse embryo. *EMBO J.* 19, 2465–2474 (2000).
- Frame, J. M., Fegan, K. H., Conway, S. J., McGrath, K. E. & Palis, J. Definitive hematopoiesis in the yolk sac emerges from Wnt-responsive hemogenic endothelium independently of circulation and arterial identity. Stem Cells 34, 431–444 (2016).
- Goldie, L. C., Lucitti, J. L., Dickinson, M. E. & Hirschi, K. K. Cell signaling directing the formation and function of hemogenic endothelium during murine embryogenesis. *Blood* 112, 3194–3204 (2008).
- Li, W., Ferkowicz, M. J., Johnson, S. A., Shelley, W. C. & Yoder, M. C. Endothelial cells in the early murine yolk sac give rise to CD41-expressing hematopoietic cells. Stem. Cells Dev. 14, 44–54 (2005).
- 53. Ning, X. et al. Divergent expression of Neurl3 from hemogenic endothelial cells to hematopoietic stem progenitor cells during development. *J. Genet. Genomics* **50**, 661–675 (2023).
- Barone, C. et al. Hemogenic endothelium of the vitelline and umbilical arteries is the major contributor to mouse fetal lymphomyelopoiesis. Preprint at *bioRxiv* https://doi.org/10.1101/2024.07. 11.603050 (2024).

- Laruy, B., Garcia-Gonzalez, I., Casquero-Garcia, V. & Benedito, R. Endothelial-to-hematopoietic transition is induced by Notch glycosylation and upregulation of Mycn. Preprint at bioRxiv https://doi.org/10.1101/2020.09.13.295238 (2020).
- 56. Ramabadran, R. et al. DNMT3A-coordinated splicing governs the stem state switch towards differentiation in embryonic and haematopoietic stem cells. *Nat. Cell Biol.* **25**, 528–539 (2023).
- Robertson, A. L. et al. Hematopoietic stem cell division is governed by distinct RUNX1 binding partners. Preprint at bioRxiv https://doi.org/10.1101/2024.06.07.596542 (2024).
- Yu, M. et al. The unique functions of Runx1 in skeletal muscle maintenance and regeneration are facilitated by an ETS interaction domain. *Development* 151 (2024).
- Azzoni, E. et al. The onset of circulation triggers a metabolic switch required for endothelial to hematopoietic transition. Cell Rep. 37, 110103 (2021).
- 60. Azzoni, E. et al. Kit ligand has a critical role in mouse yolk sac and aorta-gonad-mesonephros hematopoiesis. *EMBO Rep.* https://doi.org/10.15252/embr.201745477 (2018).
- Draper, J. E. et al. A novel prospective isolation of murine fetal liver progenitors to study in utero hematopoietic defects. *PLoS Genet.* 14, e1007127 (2018).
- 62. Kuleshov, M. V. et al. Enrichr: a comprehensive gene set enrichment analysis web server 2016 update. *Nucleic Acids Res.* **44**, W90–W97 (2016).
- Andreatta, M. & Carmona, S. J. UCell: robust and scalable single-cell gene signature scoring. Comput. Struct. Biotechnol. J. 19, 3796–3798 (2021).
- 64. Patro, R., Duggal, G., Love, M. I., Irizarry, R. A. & Kingsford, C. Salmon provides fast and bias-aware quantification of transcript expression. *Nat. Methods* **14**, 417–419 (2017).
- Soneson, C., Love, M. I. & Robinson, M. D. Differential analyses for RNA-seq: transcript-level estimates improve gene-level inferences. F1000Res 4, 1521 (2015).
- 66. Bushnell, B. BBMap: A fast, accurate, splice-aware aligner. In Proc. 9th Annual Genomics of Energy & Environment Meeting (U.S. Department of Energy Joint Genome Institute, 2014).
- Marijon, P., Chikhi, R. & Varre, J. S. yacrd and fpa: upstream tools for long-read genome assembly. *Bioinformatics* 36, 3894–3896 (2020).
- 68. Wick, R. R., Judd, L. M., Gorrie, C. L. & Holt, K. E. Completing bacterial genome assemblies with multiplex MinION sequencing. *Microb. Genom.* **3**, e000132 (2017).
- 69. Li, H. Minimap2: pairwise alignment for nucleotide sequences. *Bioinformatics* **34**, 3094–3100 (2018).
- Gleeson, J. et al. Accurate expression quantification from nanopore direct RNA sequencing with NanoCount. *Nucleic Acids Res.* 50, e19 (2022).
- Love, M. I., Huber, W. & Anders, S. Moderated estimation of fold change and dispersion for RNA-seq data with DESeq2. Genome Biol. 15, 550 (2014).

Acknowledgements

We thank the following facilities of the Cancer Research UK Manchester Institute for technical support: Advanced Imaging, Biological Resources Unit, Genome Editing and Mouse Models, Flow Cytometry and the Molecular Biology Core Facility. The Lacaud group is supported by Cancer Research UK, C5759/A20971. E.A. was supported by a Fondazione Cariplo 'Biomedical Research conducted by young researchers' grant, reference no. 2018-0102, a Leukemia Research Foundation 'New Investigator Blood Cancer Research

Grant Program', award ID 831382, a Cariplo-Telethon Alliance grant, reference no. GJC22013 and a WorldWide Cancer Research grant, reference no. 24-0083. C.B. was supported by Fondazione Umberto Veronesi. The Jacobsen group was supported by The Swedish Research Council (538-2013-8995) and the Medical Research Council (MC_UU_12009/5). We are grateful to A. Porter (CRUK-MI Research Integrity and Training Adviser) for reviewing the manuscript and providing valuable feedback. We apologize to the authors whose work we were unable to cite due to space limitations.

Author contributions

W.H.N., M.Z.H.F., H.B., R.T., M.L. and G.L. wrote the manuscript. W.H.N., M.Z.H.F., C.B., R.T., E.A., M.L. and G.L. designed experiments. W.H.N., M.Z.H.F., M.L., C.B., G.Q., F.T.F., J.C., G.S., N.M., R.T. and E.A. performed experiments. M.Z.H.F., H.B. and R.S. performed bioinformatic analyses. M.I. and S.M.B. supervised H.B.'s bioinformatic analyses. Whole-mount imaging experiments were designed performed and analyzed by C.B., G.Q., F.T.F., G.S. and E.A. VWF-reporter embryos were processed and provided by J.C. and S.E.W.J. Sequencing and library preparation was performed by J.W. and supervised by W.B. N.M. generated the Runx1 Δ exon 6 transgenic mice. M.L. and G.L. conceived and supervised the project.

Competing interests

The authors declare no competing interests.

Additional information

Extended data is available for this paper at https://doi.org/10.1038/s44161-025-00740-z.

Supplementary information The online version contains supplementary material available at https://doi.org/10.1038/s44161-025-00740-z.

Correspondence and requests for materials should be addressed to Michael Lie-A-Ling or Georges Lacaud.

Peer review information *Nature Cardiovascular Research* thanks Andrea Ditadi and the other, anonymous, reviewer(s) for their contribution to the peer review of this work.

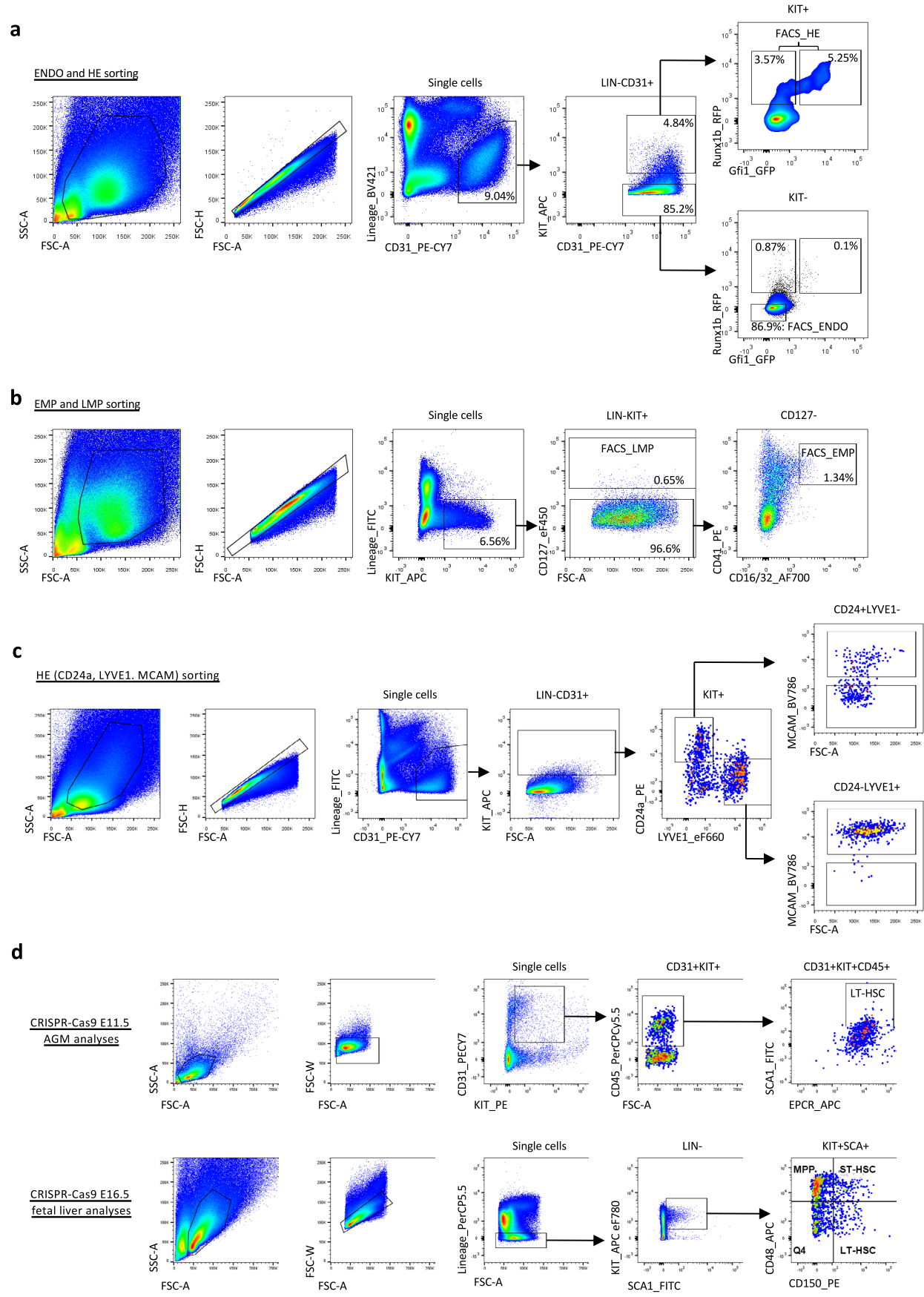
Reprints and permissions information is available at www.nature.com/reprints.

Publisher's note Springer Nature remains neutral with regard to jurisdictional claims in published maps and institutional affiliations.

Open Access This article is licensed under a Creative Commons Attribution 4.0 International License, which permits use, sharing, adaptation, distribution and reproduction in any medium or format, as long as you give appropriate credit to the original author(s) and the source, provide a link to the Creative Commons licence, and indicate if changes were made. The images or other third party material in this article are included in the article's Creative Commons licence, unless indicated otherwise in a credit line to the material. If material is not included in the article's Creative Commons licence and your intended use is not permitted by statutory regulation or exceeds the permitted use, you will need to obtain permission directly from the copyright holder. To view a copy of this licence, visit http://creativecommons.org/licenses/by/4.0/.

© The Author(s) 2025

Stem Cell Biology Group, Cancer Research UK Manchester Institute, The University of Manchester, Manchester, UK. ²Department of Oncological Sciences, Huntsman Cancer Institute, University of Utah, Salt Lake City, UT, USA. ³Division of Informatics, Imaging and Data Sciences, Faculty of Biology, Medicine and Health, The University of Manchester, Manchester, UK. ⁴School of Medicine and Surgery, University of Milano-Bicocca, Monza, Italy. ⁵Haematopoietic Stem Cell Biology Laboratory, MRC Weatherall Institute of Molecular Medicine, University of Oxford, Oxford, UK. ⁶Department of Immunology and Inflammation, Imperial College London, London, UK. ⁷Computational Biology Support, Cancer Research UK Manchester Institute, The University of Manchester, Manchester, Manchester, UK. ⁸Molecular Biology Core Facility, Cancer Research UK Manchester Institute, The University of Manchester, Manchester, UK. ⁹Genome Editing and Mouse Models, Cancer Research UK Manchester Institute, The University of Manchester, UK. ¹⁰Departamento de Biología Molecular, Facultad de Medicina, Universitat Cantabria, Santander, Spain. ¹¹Center for Hematology and Regenerative Medicine, Department of Medicine Huddinge & Department of Cell and Molecular Biology, Karolinska Institutet, Stockholm, Sweden. ¹²Department of Hematology, Karolinska University Hospital, Stockholm, Sweden. ¹³Fondazione IRCCS San Gerardo dei Tintori, Monza, Italy. ¹⁴These authors contributed equally: Wen Hao Neo, Muhammad Zaki Hidayatullah Fadlullah. ⊠e-mail: Michael.Lie-a-ling@cruk.manchester.ac.uk; Georges.Lacaud@cruk.manchester.ac.uk



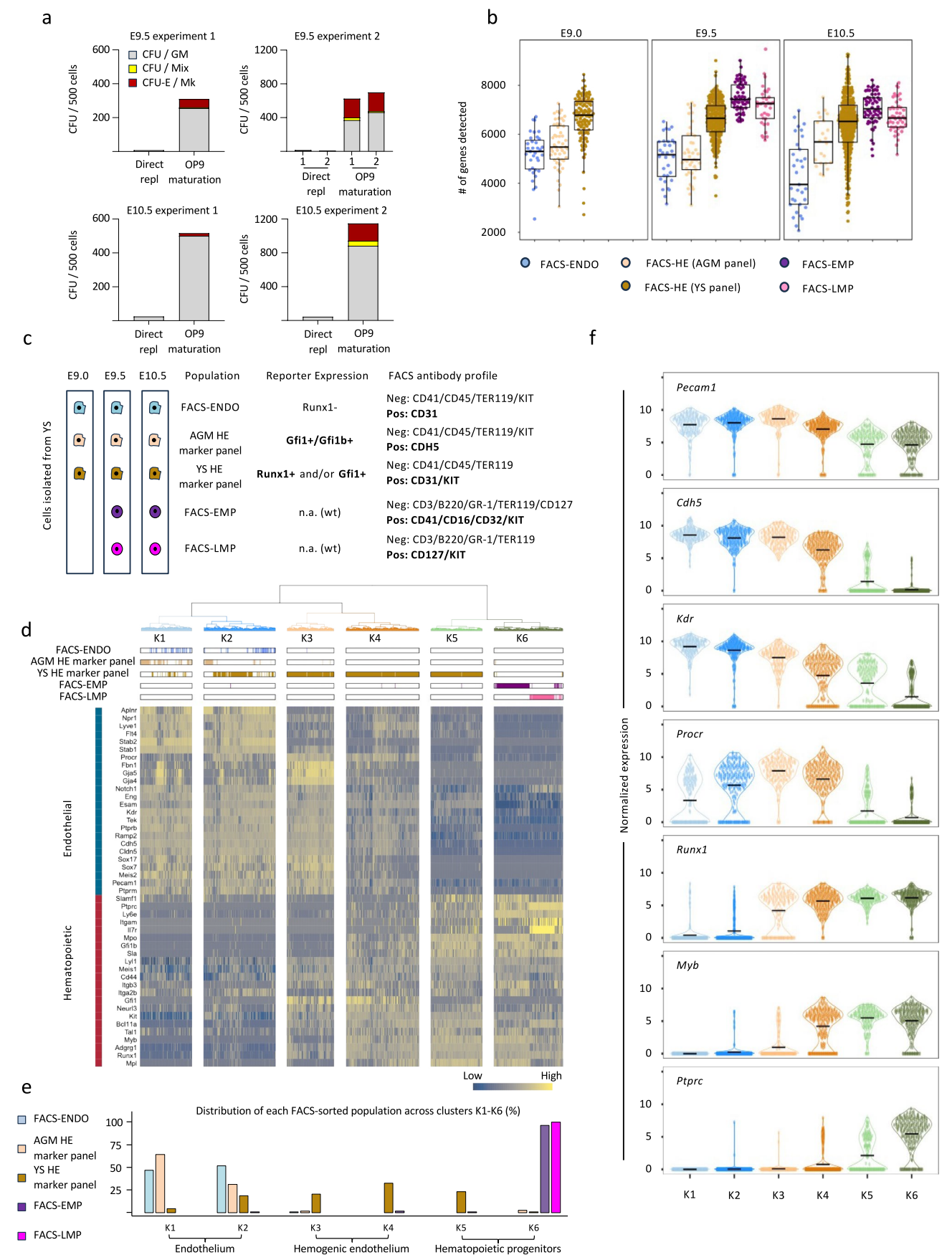
Extended Data Fig. 1 | See next page for caption.

Extended Data Fig. 1 | FACS sorting profiles used in this study. a, Gating strategy for endothelial and hemogenic endothelial sorts from yolk sac (YS). To determine which populations in the YS contain hemogenic potential, the following populations were sorted and analyzed for hematopoietic activity *in vitro*:

CD41^{neg}CD45^{neg}TER119^{neg}CD31^{pos}KIT^{neg}Runxlb:RFP^{pos} CD41^{neg}CD45^{neg}TER119^{neg} CD31^{pos}KIT^{neg}Runxlb:RFP^{pos} CD41^{neg}CD31^{pos}KIT^{pos} Runxlb:RFP^{pos} CD41^{neg}CD45^{neg}TER119^{neg}CD31^{pos}KIT^{pos} Runxlb:RFP^{pos} Gfi1:GFP^{pos} Non-hemogenic endothelial cells (FACS-ENDO) for scRNA-seq were sorted as:

CD41^{neg}CD45^{neg}TER119^{neg}CD31^{pos}KIT^{neg}Runxlb:RFP^{neg} Hemogenic endothelium enriched (FACS-HE) populations for scRNA-seq were sorted as: CD41^{neg}CD45^{neg} TER119^{neg}CD31^{pos}KIT^{pos}Runxlb:RFP^{pos}Gfi1:GFP^{pos} CD41^{neg}CD45^{neg}TER119^{neg}CD31^{pos}KIT^{pos}Runxlb:RFP^{pos}Gfi1:GFP^{pos}CD41^{neg}CD45^{neg}TER119^{neg}CD31^{pos}KIT^{pos}Runxlb:RFP^{pos}Gfi1:GFP^{pos}CD41^{neg}CD45^{neg}TER119^{neg}CD31^{pos}KIT^{pos}Runxlb:RFP^{pos}Gfi1:GFP^{pos}CD41^{neg}CD45^{neg}TER119^{neg}CD31^{pos}KIT^{pos}Runxlb:RFP^{pos}Gfi1:GFP^{pos}CD41^{neg}CD45^{neg}TER119^{neg}CD31^{pos}KIT^{pos}Runxlb:RFP^{pos}Gfi1:GFP^{pos}CD41^{neg}CD45^{neg}TER119^{neg}CD31^{pos}KIT^{pos}Runxlb:RFP^{pos}Gfi1:GFP^{pos}Gfi1:GFP^{pos}CD41^{neg}CD45^{neg}TER119^{neg}CD31^{pos}KIT^{pos}Runxlb:RFP^{pos}Gfi1:GFP^{pos}Gfi1:GFP^{pos}CD41^{neg}CD45^{neg}TER119^{neg}CD31^{pos}KIT^{pos}Runxlb:RFP^{pos}Gfi1:GFP^{pos}Gfi1:GFP^{pos}CD41^{neg}CD45^{neg}TER119^{neg}CD31^{pos}KIT^{pos}Runxlb:RFP^{pos}Gfi1:GFP^{pos}Gfi1:GFP^{pos}CD41^{neg}CD45^{neg}TER119^{neg}CD31^{pos}KIT^{pos}Runxlb:RFP^{pos}Gfi1:GFP^{pos}Gfi1:GFP^{pos}CD41^{neg}CD45^{neg}TER119^{neg}CD31^{pos}KIT^{pos}Runxlb:RFP^{pos}Gfi1:GFP^{pos}Gfi1:GFP^{pos}DsGfi1:GFP^{pos}CD41^{neg}CD45^{neg}TER119^{neg}CD31^{pos}KIT^{pos}Runxlb:RFP^{pos}Gfi1:GFP^{pos}CD41^{neg}CD45^{neg}TER119^{neg}CD31^{pos}KIT^{pos}Runxlb:RFP^{pos}Gfi1:GFP^{pos}CD41^{neg}CD45^{neg}TER119^{neg}CD31^{pos}KIT^{pos}Runxlb:RFP^{pos}Gfi1:GFP^{pos}CD41^{neg}CD45^{neg}CD45^{neg}CD45^{neg}CD45^{neg}CD45^{neg}CD45^{neg}

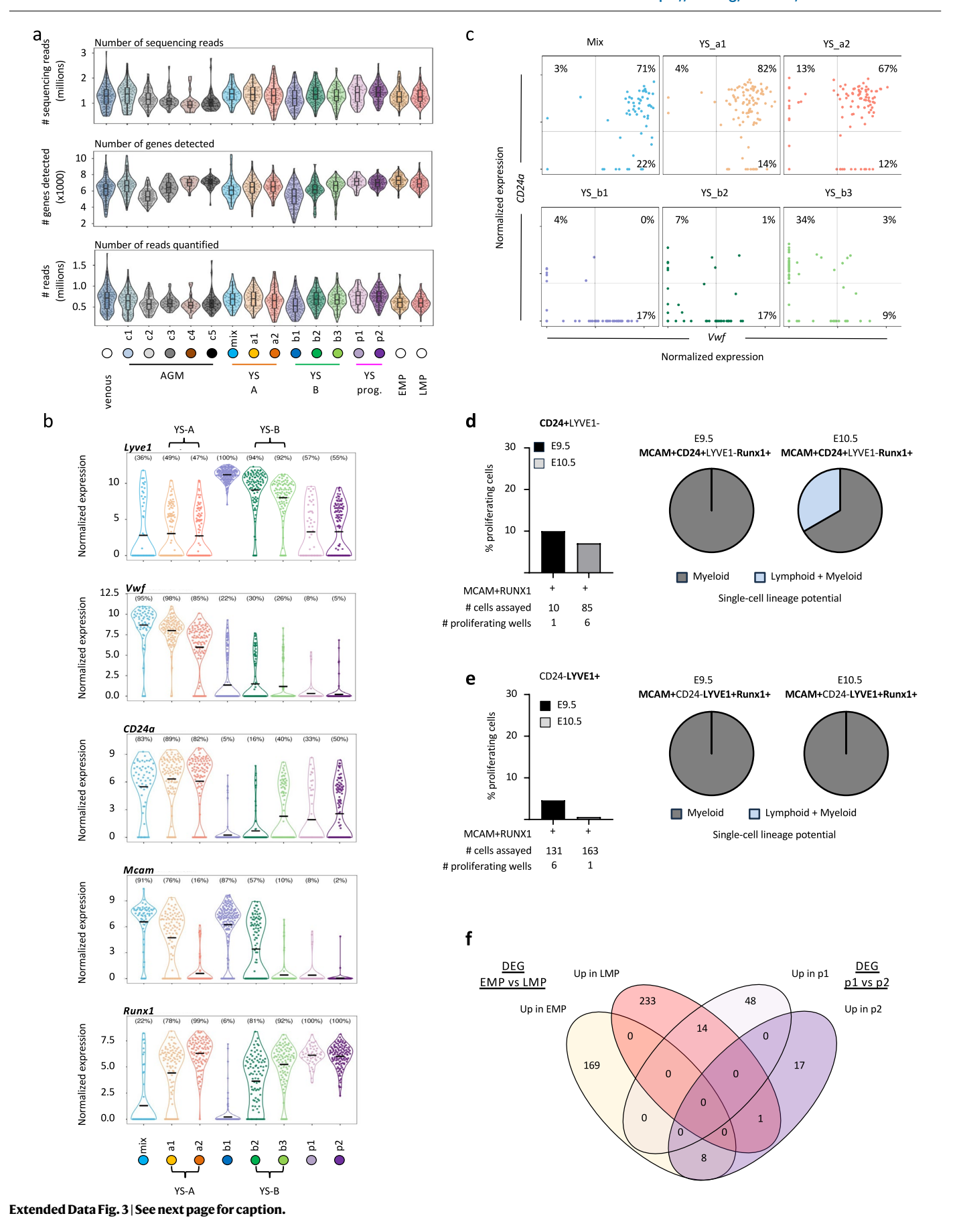
progenitors (LMP) sorts from YS. FACS-EMP: CD3^{neg}B220^{neg}GR1^{neg}TER119^{neg}KIT^{pos} CD127^{neg}CD41^{pos}CD16/32^{pos}. Bertrand, J.Y. et al. Blood 106, 3004-3011 (2005). Frame, J.M., Fegan, K.H., Conway, S.J., McGrath, K.E. & Palis, J. Stem Cells 34, 431-444, 2016. FACS-LMP: CD3^{neg}B220^{neg}Gr1^{neg}TER119^{neg}KIT^{pos}CD127^{pos} Boiers, C. et al. Cell Stem Cell 13, 535-548, 2013. Yoshimoto, M. et al. Proc Natl Acad Sci U S A 108, 1468-1473, 2011. c, Gating strategy to enrich for HE with LMP potential and HE with EMP potential from YS. FACS-HE^{LMP}:CD41^{neg}CD45^{neg} TER119^{neg} CD31^{pos}KIT^{pos}CD24a^{pos}LYVE1^{neg}MCAM^{neg} FACS-HE^{EMP}:CD41^{neg}CD45^{neg} TER119^{neg} CD31^{pos}KIT^{pos}CD24a^{neg}LYVE1^{pos}MCAM^{neg} d, Gating strategy to analyze phenotypic long-term HSC (LT-HSC) and emerging hematopoietic cells (CD31^{pos}KIT^{pos}CD45^{pos}) in E11.5 AGM regions and long-term HSC (LT-HSC) in E16.6 fetal livers. LT-HSC (AGM): CD31^{pos}SCA^{pos}KIT^{pos}CD45^{pos}EPCR^{pos}. LT-HSC (fetal liver): B220^{neg}CD3^{neg}GR1^{neg}TER119^{neg}CD48^{neg}SCA^{pos}KIT^{pos}CD150^{pos}.



Extended Data Fig. 2 | See next page for caption.

Extended Data Fig. 2 | Identification of HE activity in KIT^{pos}Runx1^{pos}
CD31^{pos}LIN^{neg} extra-embryonic cells for single-cell profiling of extraembryonic EHT. a, Hematopoietic colony forming unit (CFU) assay on
KIT^{pos}Runx1^{pos}CD31^{pos}LIN^{neg} extra-embryonic cells FACS-isolated from Runx1^{RFP}
reporter mice. Cells were either directly replated, or co-cultured with OP9 feeder
cells for 48 h before replating. Hematopoietic colonies were quantified after
10 days. Individual CFU assays are shown. N = 2 biological experiments. E/Mk =
Erythrocyte/Megakaryocyte, Mix = Granulocyte/Erythrocyte/Macrophage/
Megakaryocyte, G/M = Granulocyte/Macrophage. b, Numbers of genes
detected and the number of cells that passed QC within each FACS-sorted
population from dissected E9.0, E9.5 and E10.5 YS (full-length scRNA-seq,
Smart-seq2). Embedded boxplots indicate the median (horizontal line), the
upper and lower hinges represent the 75th and 25th percentile and whiskers
extend to 1.5x the inter-quartile range. c, Schematic of the cell populations

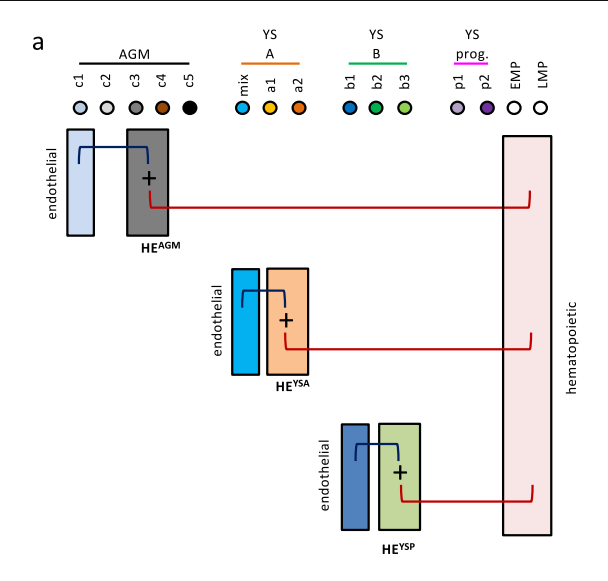
FACS-sorted from dissected E9, E9.5 and E10.5 YS and processed for full-length single-cell Smart-seq2 RNA sequencing. Endo: endothelium, AGM HE marker panel (CD41^{neg}CD45^{neg}TER119^{neg}CDH5^{pos}KIT^{neg}Gfi1/Gfi1b^{pos}), YS HE marker panel (CD41^{neg} CD45^{neg} TER119^{neg}CD31^{pos}KIT^{neg}Runx1/Gfi1^{pos}), EMP: erythro-myeloid progenitor, LMP: lympho-myeloid progenitor. d, Tree dendrogram generated by hierarchical clustering of the sorted populations in (c). Below the dendrogram, the contribution of the different FACS-sorted populations to each cluster is shown. All cells sorted from the YS using the AGM HE marker panel cluster together with YS FACS-ENDO cells. Bottom: heatmap depicting the expression of endothelial (top) and hematopoietic (bottom) genes across clusters K1-K6 e, Bar graph depicting the distribution (as percentage) of each FACS-sorted population listed in (c) across clusters K1-K6. f, Violin plots depicting the expression of selected endothelial (*Pecam1*, *Cdh5*, *Kdr*, *Procr*) and hematopoietic genes (*Runx1*, *Myb*, *Ptprc*) across clusters K1-K6. Black bars represent the mean expression level.

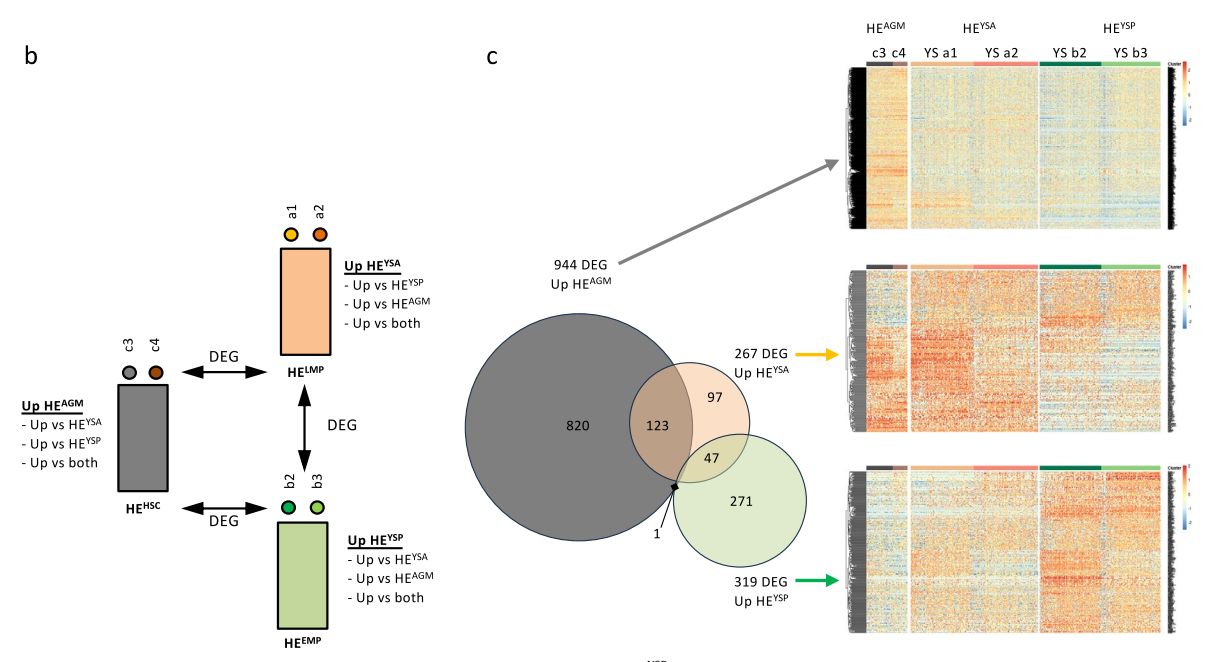


Extended Data Fig. 3 | Two distinct extra-embryonic EHT trajectories.

a, Violin plots depicting the # of sequencing reads, # of genes detected, # of reads quantified for all scRNA-seq clusters/populations analyzed in this study. Embedded boxplots indicate the median (horizontal line), the upper and lower hinges represent the 75th and 25th percentile and whiskers extend to 1.5x the inter-quartile range. The AGM-derived part of the dataset is described in depth in Fadlullah, M.Z.H. et al. *Blood* 139, 343-356, 2022. **b**, Violin plots depicting the expression of candidate genes for immunofluorescence- based analyses of the YS-middle and YS-bottom clusters. **c**, Top: Correlation between transcript expression of *CD24a* and *Vwf* in YS-middle trajectory clusters (mix-m1-m2) and YS-bottom trajectory clusters (b1-b2-b3). Both *Vwf* and *CD24a* are selective for clusters mix, m1 and m2. **d**, Left: Single-cell hematopoietic assays of early YS-middle cells (likely cluster m1) (KIT^{pos}CD31^{pos}LIN^{neg}LYVE1^{neg}CD24^{pos}MCAM^{pos}Runx1:RFP^{pos}) cultured on OP9 feeder cells for 14 days. The percentage of

wells containing proliferating hematopoietic cells is shown. Right: Lineage distribution of the hematopoietic cells shown in the left panel, as determined by flow cytometry for myeloid (GRI, MACI/CDI1b), erythroid (TERI19) and lymphoid (CD19) markers. No erythropoiesis was observed. e, Left: Single-cell hematopoietic assays of early YS-bottom cells (likely cluster b2) (KIT^{pos}CD31^{pos} LIN^{neg}LYVE1^{pos}CD24^{neg}MCAM^{pos}Runx1:RFP^{pos}) cultured on OP9 feeder cells for 14 days. The percentage of wells containing proliferating hematopoietic cells is shown. Right: Lineage distribution of the hematopoietic cells shown in the left panel, as determined by flow cytometry for myeloid (GRI, MACI/CDI1b), erythroid (TERI19) and lymphoid (CD19) markers. No erythropoiesis was observed. f, EMP-fate (8 genes) and LMP-fate (14 genes) signatures were extracted by intersecting pairwise differential gene expression results (EMP vs LMP and P1 vs P2). Fate signatures are listed in Supplementary Table 1.

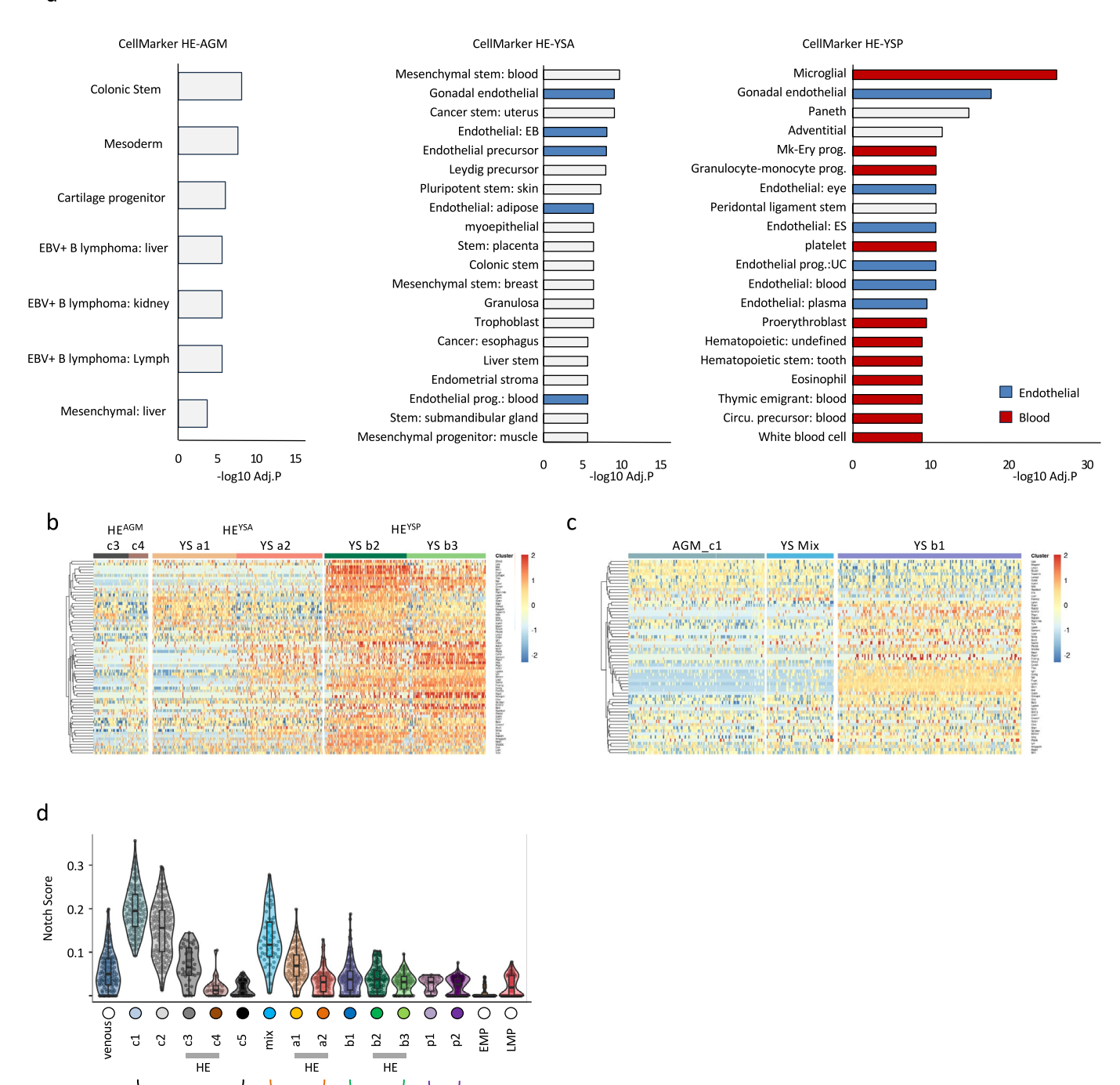




 $\label{eq:continuous} \textbf{Extended Data Fig. 4} \ | \ Shared \ and \ Unique \ HE \ profiles. \ a, \ Schematic \ depicting \ which \ differential \ gene \ expression \ (DEG) \ lists \ (log2FC>1) \ were \ used to \ establish the shared \ HE \ profiles. \ b, \ Schematic \ depicting \ how \ unique \ HE \ profiles \ were \ established \ using \ pairwise \ comparison \ between the three \ HE \ populations. \ HE^{AGM} \ (clusters \ c3 \ and \ c4 \ from \ the \ AGM), \ HE^{YSA} \ (clusters \ a1 \ and \ a2 \ from \ the \ YS),$

HE^{YSP} (clusters b2 and b3 from the YS). **c**, Left: Venn diagram depicting the result of pairwise DEG analysis on HE^{AGM}, HE^{YSA} and HE^{YSP}. "Up" indicates a gene is upregulated (log2FC > 1.5) vs at least one other HE. The genes present in each group are depicted in the single-cell heatmaps on the right. Genes up in HE^{YSP} show a high overlap with HE^{AGM} gene hits.

а



Extended Data Fig. 5 | **unique HE profiles. a**, CellMarker analysis on the DEG between the three HE populations. Top hits in the CellMarker database are shown (capped at 20). Genes upregulated in HE $^{\rm YSP}$ have a strong hematopoietic identity. This is not observed in any of the other HE populations. Adjusted p-values were calculated using Fisher's exact test with Benjamini–Hochberg correction. **b**, Single-cell heatmap of hematopoietic genes, extracted from the HE $^{\rm YSP}$ Cellmarker analysis in (a), across three HE populations. **c**, Single-cell heatmap of hematopoietic gene expression, extracted from the HE $^{\rm YSP}$ CellMarker analysis

YS A

YS B

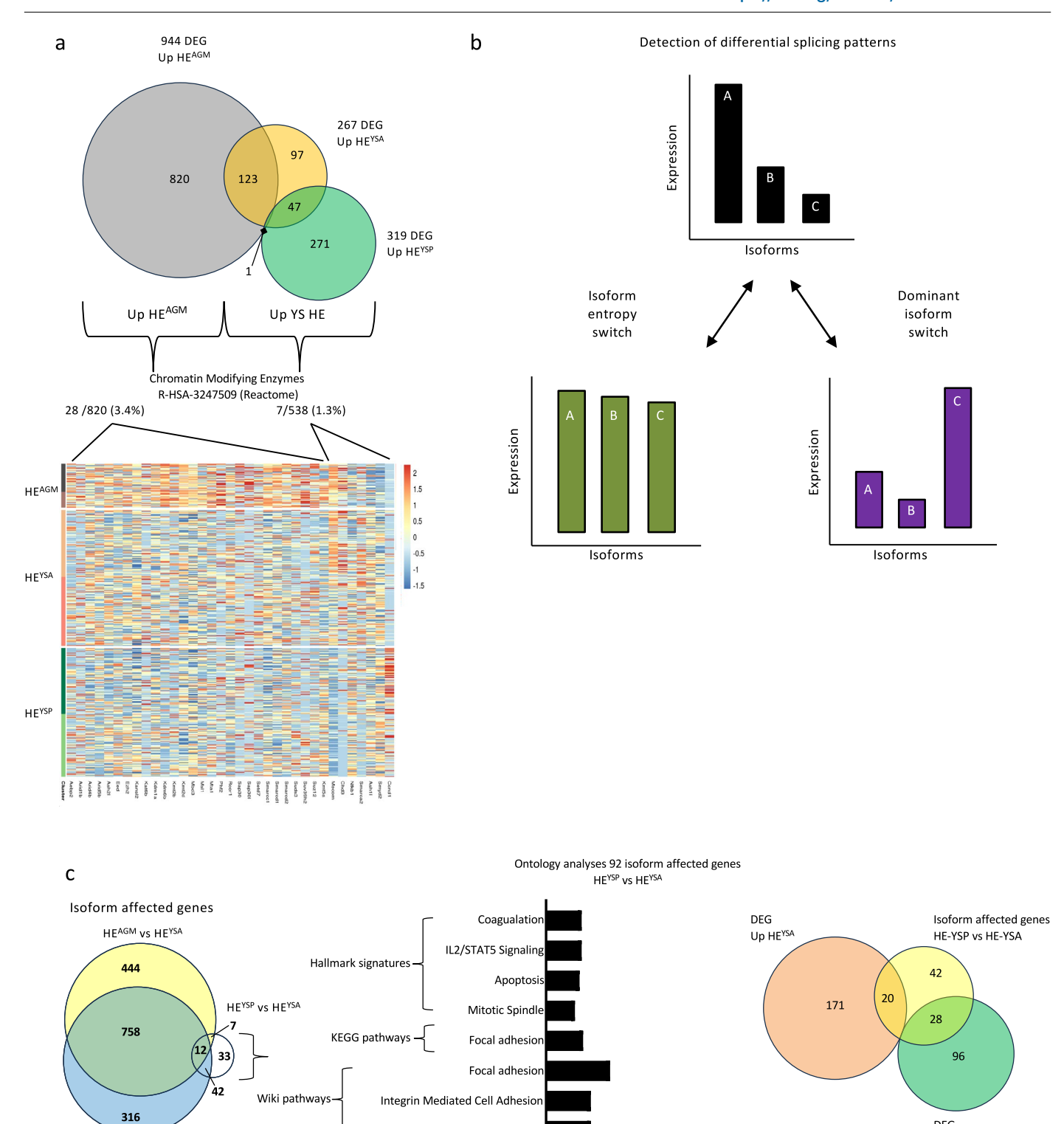
YS prog.

AGM

in (a), across non-HE endothelial populations. Plexus endothelium expresses relatively high levels of hematopoietic genes compared to the other endothelial populations. **d**, Violin plots depicting Notch signature scores across all clusters defined in main Fig. 2b. For reference, AGM-derived venous endothelial cells (left column) and extra-embryonic-derived EMP and LMP populations (right columns) are also included. Embedded boxplots indicate the median (horizontal line), the upper and lower hinges represent the 75th and 25th percentile and whiskers extend to 1.5x the inter-quartile range.

DEG

Up HE^{YSP}



IL3 Signaling Pathway

4 6

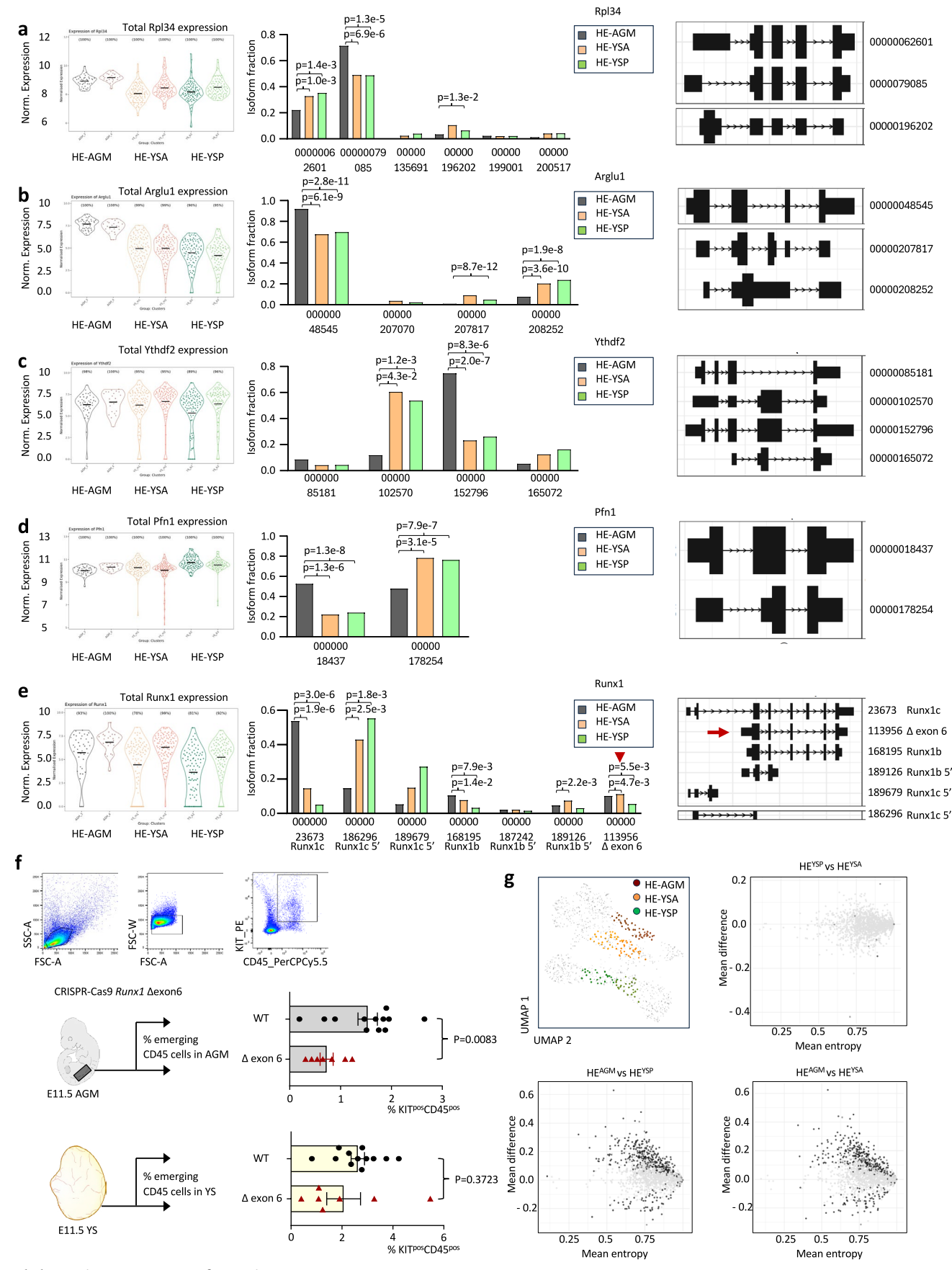
8 10 -log10 Adj.P

Extended Data Fig. 6 | See next page for caption.

HE^{AGM} vs HE^{YSP}

Extended Data Fig. 6 | Enrichment of Chromatin modifiers in HE^{AGM} **and isoform level analyses of HE populations. a**, Top: Venn diagram depicting the result of pairwise DEG analysis on HE^{AGM}, HE^{YSA} and HE^{YSP}. "Up" indicates a gene is upregulated (> logfc1.5) vs at least one other HE. Bottom single-cell heatmap depicting the genes from Chromatin Modifying Enzymes R-HSA-3247509 (Reactome) that are differentially expressed between the HE populations. **b**, Schematic representation of different isoform usage patterns. Left: schematic representation of isoform Mean Entropy Differences (MED). Right: Schematic representation of dIF (difference in Isoform Fraction) changes **c**, Analyses of isoform differences (entropy and/or dIF) between HE^{AGM} vs HE^{YSP}, HE^{AGM} vs HE^{YSA}

and HE^{YSP} vs HE^{YSA}. Left: Ven diagram depicting the intersect of the different comparisons. Only a small set of 94 genes show isoform level differences between the HE^{YSA} vs HE^{YSP}. Middle: Gene ontology analyses across Wikipathways 2024 Mouse, KEGG 2021 human and MSigDB Hallmark 2020 databases. The input gene lists consisted of the 92 genes that showed differential isoform expression (entropy and/or dIF) between HE^{YSA} and HE^{YSP}. All significant hits are shown. Gene lists can be interrogated in Supplementary Table 4. Adjusted p-values were calculated using Fisher's exact test with Benjamini–Hochberg correction. Right: Ven diagram showing the overlap of the isoform affected genes and genes that are differentially expressed between the two YS HE populations (HE^{YSA} and HE^{YSP}).



 $\textbf{Extended Data Fig. 7} \, | \, \textbf{See next page for caption.} \\$

Extended Data Fig. 7 | The unique isoform landscape of HE^{AGM} , a-e, gene and isoform expression for Rpl34 (a), Arglu1 (b), Ythdf2 (c), Pfn1 (d) and Runx1 (e). Left: violin plot of single cell normalized (total) gene expression in HE^{AGM} (clusters c3-c4), HE^{YSA} (clusters a1-a2) and HE^{YSP} (cluster b2-b3), Middle: isoform usage bar graph depicting all detected isoforms (ENSMUST). Statistical test used was the IsoformSwitchAnalyzeR implementation of the DTU test in the satuRn R package [https://f1000research.com/articles/10-374/v2] (a generalized linear model-based test). Right: schematic of relevant isoforms. The red arrow in (e) highlights the Runx1 isoform that lacks exon 6. f, Emerging hematopoietic cells (KITPosCD45Pos) in E11.5 wildtype and CRISPR-Cas9 Runx1 Δ exon 6 embryos identified by flow cytometry. Top, representative analysis flow cytometry plots. Middle, the percentage of KITPosCD45Pos cells in E11.5 AGM regions. Each point represents a single AGM. Bottom, the percentage of KITPosCD45Pos cells in

E11.5 Yolk sacs. Each point represents a single yolk sac. WT N = 12, Δ exon 6 N = 7. Bars represent the average + s.e.m. Statistical test: unpaired two-tailed t-test. ${\bf g}$, Nanopore long-read sequencing of embryonic HE populations. Top right: single cell UMAP depicting three embryonic EHT trajectories as depicted and described in main Fig. 2a-b. The dots indicate 160 cells that have been resequenced on the nanopore long-read platform. Right and bottom: Analyses of isoform entropy difference between HE^YSP vs HE^YSA, HE^AGM vs HE^YSP and HE^AGM vs HE^YSA and. Left: scatter plots showing the genes having differential usage pattern for the indicated comparison. Black dots represent genes with significant mean entropy differences (mean difference > 0.1, FDR adjP < 0.05). Statistical test: Wilcoxon signed-rank test, two-tailed. Gray dots represent genes with non-significant changes.

nature portfolio

Corresponding author(s):	Michael Lie-A-Ling, Georges Lacaud
Last updated by author(s):	Sep 18, 2025

Reporting Summary

Nature Portfolio wishes to improve the reproducibility of the work that we publish. This form provides structure for consistency and transparency in reporting. For further information on Nature Portfolio policies, see our <u>Editorial Policies</u> and the <u>Editorial Policy Checklist</u>.

For all statistical analyses, confirm that the following items are present in the figure legend, table legend, main text, or Methods section.

Statistics

n/a	Confirmed
	The exact sample size (n) for each experimental group/condition, given as a discrete number and unit of measurement
	A statement on whether measurements were taken from distinct samples or whether the same sample was measured repeatedly
	The statistical test(s) used AND whether they are one- or two-sided Only common tests should be described solely by name; describe more complex techniques in the Methods section.
\boxtimes	A description of all covariates tested
	A description of any assumptions or corrections, such as tests of normality and adjustment for multiple comparisons
	A full description of the statistical parameters including central tendency (e.g. means) or other basic estimates (e.g. regression coefficient) AND variation (e.g. standard deviation) or associated estimates of uncertainty (e.g. confidence intervals)
	For null hypothesis testing, the test statistic (e.g. <i>F</i> , <i>t</i> , <i>r</i>) with confidence intervals, effect sizes, degrees of freedom and <i>P</i> value noted <i>Give P values as exact values whenever suitable.</i>
\boxtimes	For Bayesian analysis, information on the choice of priors and Markov chain Monte Carlo settings
	For hierarchical and complex designs, identification of the appropriate level for tests and full reporting of outcomes
	Estimates of effect sizes (e.g. Cohen's d, Pearson's r), indicating how they were calculated

Software and code

Policy information about availability of computer code

Data collection Zeiss Zen software version 2.3 SP1;

IMARIS Viewer software version 9.7.2 (Bitplane), ImageJ/Fiji (versions 2.3.5-2.9.0) and Adobe Photoshop 504 CC 2021.

Fiji/ImageJ Cell Counter tool

FlowJo (v10.1)

Data analysis

Zeiss Zen software version 2.3 SP1;

IMARIS Viewer software version 9.7.2 (Bitplane),

ImageJ/Fiji (versions 2.3.5-2.9.0) and Adobe Photoshop 504 CC 2021.

Fiji/ImageJ Cell Counter tool

FlowJo (v10.1)

bcltoFastq conversion (version 2.20.0.422)

STAR aligner (version 2.7.9a)

R (version 4.1.0)

Bioconducter package DropletUtils (version 1.12.1).

SingleCellExperiment (version 1.14.1)

Seurat (version 4.0.6).

Scater (version 1.20.1)

buildSNNGraph

scanpy workflow (version 1.6.1)

'limma' package (version 3.54.2)

UCell package128 (version 2.2.0)
splice aware aligner Salmon 1.4.0
IsoformSwitchAnalyzeR 2.01.07
SplicingFactory 1.8.0
DESeq2 1.40.2
MinionQC.R 1.4.2131
MinKNOW 23.04.6
Guppy 6.5.7
Minimap2 2.26
IGV Desktop App 2.17.0
ChIPpeakAnno version 3.20.1
https://github.com/zakiF/PublishedPapers/tree/master/YolkSac_AGM
https://github.com/RASellers-CRUK/GL_IsoformAnalysis

For manuscripts utilizing custom algorithms or software that are central to the research but not yet described in published literature, software must be made available to editors and reviewers. We strongly encourage code deposition in a community repository (e.g. GitHub). See the Nature Portfolio guidelines for submitting code & software for further information.

Data

Policy information about availability of data

All manuscripts must include a data availability statement. This statement should provide the following information, where applicable:

- Accession codes, unique identifiers, or web links for publicly available datasets
- A description of any restrictions on data availability
- For clinical datasets or third party data, please ensure that the statement adheres to our policy

The following published datasets were used in this study:
GEO
GSE137116
GSE139389
GSE167588
GSE173833
GSM5281418
GSE57251
GSM1377856
GSM1377857
GSM1377858
GSE22178
GSE69101
GSM1692809
GSM1692853
GSM1692854
GRCm39 M33 mouse reference
GRCm39 M32 mouse reference
mm10 reference
For the data generated in this study:
Gene expression data can be queried at https://shiny.cruk.manchester.ac.uk/AGM_YS_dataset_final/. Raw data is deposited in GEO accession GSE274544 and
GSE309071. Three source data files accompany this manuscript
NCVR_2024_09_0957A_extended_source.xlsx, NCVR_2024_09_0957A_main_source.xlsx and NCVR_2024_09_0957A supplemental_tables_1.xlsx
Code used:
$https://github.com/zakiF/PublishedPapers/tree/master/YolkSac_AGM and https://github.com/RASellers-CRUK/GL_lsoformAnalysis https://github.com/RASellers-CRUK/GL_lsoformAnalysis https://github$

Research involving human participants, their data, or biological material

Policy information about studies with <u>human participants or human data</u>. See also policy information about <u>sex, gender (identity/presentation)</u>, <u>and sexual orientation</u> and <u>race, ethnicity and racism</u>.

Reporting on sex and gender	NA
Reporting on race, ethnicity, or other socially relevant groupings	NA
Population characteristics	NA
Recruitment	NA
Ethics oversight	NA

Note that full information on the approval of the study protocol must also be provided in the manuscript.

Field-specific reporting		
Please select the or	ne below that is the best fit for your research. If you are not sure, read the appropriate sections before making your selection.	
Life sciences	Behavioural & social sciences Ecological, evolutionary & environmental sciences	
For a reference copy of t	of the document with all sections, see nature.com/documents/nr-reporting-summary-flat.pdf	
Life scier	nces study design	
All studies must dis	close on these points even when the disclosure is negative.	
Sample size	No statistical methods were used to predetermine sample size. For in vivo transplantation experiments, five mice per group were used.	
Data exclusions	All replicate data were used for statistical analysis and no data were excluded.	
Replication	All data were replicated at least one time (N=2 biological experiments)	
Randomization	Samples were randomly allocated into experimental groups and processed in no particular order to minimize batch effects.	
Blinding	The investigators were not blinded to group allocation during data collection and analysis.	

Reporting for specific materials, systems and methods

We require information from authors about some types of materials, experimental systems and methods used in many studies. Here, indicate whether each material, system or method listed is relevant to your study. If you are not sure if a list item applies to your research, read the appropriate section before selecting a response.

Ma	terials & experimental systems	Me	thods
n/a	Involved in the study	n/a	Involved in the study
	Antibodies	\boxtimes	ChIP-seq
	Eukaryotic cell lines		
\boxtimes	Palaeontology and archaeology	\boxtimes	MRI-based neuroimaging
	Animals and other organisms		
\boxtimes	Clinical data		
\boxtimes	Dual use research of concern		
\boxtimes	Plants		

Antibodies

Antibodies used

Antibody Clone Manufacturer Application dilution Experiment B220 APC RA3-6B2 eBioscience FACS 1:200 Co-culture readout B220 eF450 RA3-6B2 eBioscience FACS 1:400 Co-culture readout B220 FITC RA3-6B2 Invitrogen FACS 1:400 YS lineage staining B220 Biotin RA3-6B2 eBioscience FACS 1:200 FL HSC staining, FACS sort LT-HSC CD16/CD32 93 Invitrogen FACS 1:100 Fc blocking CD16/CD32 AF700 93 eBioscience FACS 1:200 YS EMP/LMP staining CD19 APC eF780 eBio1D3 eBioscience FACS 1:200 Co-culture readout CD19 PE-Cy7 eBio1D3 eBioscience FACS 1:200 terminal BM samples CD24a PE 30-F1 eBioscience FACS 1:200 YS EHT staining CD24a PerCPCy5.5 M1/69 BD FACS 1:200 YS EHT staining CD25 Biotin eBio7D4 eBioscience FACS 1:200 Co-culture readout CD3 APC 145-2C11 eBioscience FACS 1:200 terminal BM samples CD3 FITC 145-2C11 eBioscience FACS 1:400 YS lineage staining CD3 biotin 145-2C11 eBioscience FACS 1:200 FL HSC staining, FACS sort LT-HSC CD31 PECy7 390 BioLegend FACS 1:200 YS EHT, AGM-HSC staining CD41 APC MWReg30 eBioscience FACS 1:200 AGM /YS lineage staining CD41 Biotin MWReg30 eBioscience FACS 1:400 AGM /YS lineage staining CD41 FITC MWReg30 eBioscience FACS 1:400 AGM /YS lineage staining CD41 PE MWReg30 eBioscience FACS 1:200 YS EHT staining CD41 PECy7 MWReg30 eBioscience FACS 1:200 YS EMP/LMP staining CD45 Biotin 30-F11 Invitrogen FACS 1:400 AGM /YS lineage staining CD45 FITC 30-F11 Invitrogen FACS 1:400 AGM /YS lineage staining CD45 PerCPCy5.5 30-F11 eBioscience FACS 1:400 Co-culture readout, AGM-HSC staining

```
CD45.1 APC- Efl 780 A20 eBioscience FACS 1:400 peripheral blood analysis
CD45.2 PerCp 5.5 104 eBioscience FACS 1:400 peripheral blood analysis
CD127 eF450 A7R34 eBioscience FACS 1:100 YS EMP/LMP staining
CD127 PE A7R34 Invitrogen FACS 1:100 YS EMP/LMP staining
CD48 APC, FACS sort LT-HSC HM48-1 eBioscience FACS 1:200 FL HSC staining
CD150 PE-Cy7 TC15-12F12.2 BioLegend FACS 1:400 FACS sort LT-HSC
CD150 PE TC15-12F12.2 BioLegend FACS 1:400 FL HSC staining
CD201 (EPCR, ProcR) APC eBio1560 eBioscience FACS 1:200 AGM-HSC
c-Kit APC 2B8 eBioscience FACS 1:400 AGM/YS EHT staining
c-KIT PE 2B8 eBioscience FACS 1:400 AGM-HSC / AGM staining
c-Kit APC eF780 2B8 eBioscience FACS 1:200 AGM/YS EHT, AGM-HSC and FL HSC staining
c-Kit SB436 2B8 eBioscience FACS 1:600 AGM/YS EHT staining
Ly-6G / Gr1 APC RB6-8C5 eBioscience FACS 1:400 Co-culture readout
Ly-6G / Gr1 FITC RB6-8C5 eBioscience FACS 1:400 YS lineage staining
Ly-6G / Gr1 PECy7 RB6-8C5 eBioscience FACS 1:200 Co-culture readout
LYVE1 eF660 ALY7 eBioscience FACS 1:10000 YS EHT staining
Ly-6G / Gr1 biotin RB6-8C5 eBioscience FACS 1:200 Fetal liver HSC, FACS sort LT-HSC
CD11b / Mac1 APC M1/70 eBioscience FACS 1:400 Co-culture readout
CD11b / Mac1 PE M1/70 eBioscience FACS 1:200 Co-culture readout
CD146 / MCAM Biotin ME-9FI BD FACS 1:200 YS EHT staining
CD146 / MCAM BV786 ME-9FI BD FACS 1:200 YS EHT staining
NK1.1 PerCpCy5.5 PK136 eBioscience FACS 1:200 Co-culture readout
Ly-6A/E (Sca-1)-FITC E13-161.7 BD FACS 1:200 AGM-HSC, Fetal liver HSC
Streptavidin BV421 Biolegend FACS 1:400 AGM/YS EHT staining
Streptavidin PerCP5.5 eBioscience FACS 1:200 Fetal liver HSC
SYTOX Green Invitrogen FACS 1:1000 Viability dye
TER119 Biotin TER-119 Biolegend FACS 1:400 AGM /YS lineage staining, FACS sort LT-HSC
TER119 BV650 TER-119 Biolegend FACS 1:100 Co-culture readout
TER119 FITC TER-119 Biolegend FACS 1:400 AGM /YS lineage staining
TER119 PE TER-119 Biolegend FACS 1:200 Co-culture readout
Thy1.2 (CD90.2) SB600 53-2.1 Invitrogen FACS 1:200 Co-culture readout
Lyve1 AF2125 R&D Systems Whole mount IF 1:200 detection of HE-EMP
Runx1+Runx2+Runx3 EPR3099 Abcam Whole mount IF 1:400 detection of HE
GFP A10262 Invitrogen Whole mount IF 1:500 detection of Vwf:GFP reporter
anti goat Alexa Fluor Plus 647 A32849 Invitrogen Whole mount IF 1:500 detection of LYVE1
anti rabbit Alexa Fluor 555 A32794 Invitrogen Whole mount IF 1:500 detection of RUNX
anti chicken Alexa Fluor 488 A78948 Invitrogen Whole mount IF 1:500 detection of GFP
```

Validation

Wild animals

All antibodies used have been validated by the manufacturers for their respective applications.

Eukaryotic cell lines

Policy information about <u>cell lines and Sex and Gender in Research</u>

Cell line source(s)

OP9 cells (mouse bone marrow stromal cell line; ATCC® CRL-2749™) were obtained from the American Type Culture Collection (ATCC, Manassas, VA, USA).

Collection (ATCC, Ivialiassas, VA, OSA)

Authentication not done

Mycoplasma contamination not tested

Commonly misidentified lines (See ICLAC register)

Animals and other research organisms

Policy information about <u>studies involving animals</u>; <u>ARRIVE guidelines</u> recommended for reporting animal research, and <u>Sex and Gender in Research</u>

Laboratory animals mouse embryos E9 - E16, were genereated from crosses between reporter male (C57BL/6JOlaHsd) mice and wt female Hsd:ICR (CD-1®) mice. For transplantations NSGS (NOD.Cg-Prkdcscid II2rgtm1Wjl Tg(CMV-IL3,CSF2,KITLG)1Eav/MloySzJ) mice (CD45.1) aged

8-12 weeks were used.

No

Reporting on sex Embryos were not sexed. adult transplant recipient were female

Field-collected samples na

Ethics oversight Mouse work was performed in accordance with the United Kingdom Animal Scientific Procedures Act (ASPA) 1986. Animal experiments performed at the Cancer Research United Kingdom Manchester Institute (CRUK-MI) were approved by the Animal

Welfare and Ethics Review Body (AWERB) of the CRUK-MI. Experiments performed at the University of Oxford were approved by the Oxford Clinical Medicine Ethical Review Committee.

Note that full information on the approval of the study protocol must also be provided in the manuscript.

_			
D	2	n	to

Seed stocks	na
Novel plant genotypes	na
Authentication	na

Flow Cytometry

Plots

Confirm that:

- The axis labels state the marker and fluorochrome used (e.g. CD4-FITC).
- The axis scales are clearly visible. Include numbers along axes only for bottom left plot of group (a 'group' is an analysis of identical markers).
- All plots are contour plots with outliers or pseudocolor plots.
- A numerical value for number of cells or percentage (with statistics) is provided.

Methodology

Sample preparation

For the single cell RNA-seq and in vitro functional assays, dissected yolk-sacs were digested in a mix of Collagenase IV (2 mg/ ml, Worthington) and DNase I (200 U/ml, Calbiochem) at 37 °C for 15 min. The dissociated cells were pelleted (300 g for 5 min at 4°C) and resuspended in phosphate buffered saline containing 10% fetal bovine serum (10% FBS in PBS) and further processed for FACS-analyses/sorting. E16.5 Fetal livers, dissected livers were crushed with the end of a 1ml syringe through a 40um cell strainer into IMDM+10% FBS. Dissected AGM tissues at E10.5 were finely chopped and the obtained fragments were digested in a mix of Collagenases IV (2 mg/ml, Worthington) and DNase I (200 U/ml, Calbiochem) at 37 °C with gentle agitation for 15 min. The dissociated cells were centrifuged at 300 g for 6 min and resuspended in PBS supplemented with

All flow cytometry analyses was performed on a BD LSRFortessa™ X-20 Cell Analyzer (BD Biosciences) or Novocyte Quanteon (Agilent). All cell sorting was performed on a BD FACSAria™ III Cell Sorter (BD Biosciences). Antibodies used for FACS are listed in table 5. For scRNA-seq cells were directly sorted into lysis buffer and snap-frozen before further processing. FlowJo software (BD Biosciences) was used to analyze all FACS data.

Instrument

BD LSRFortessa™ X-20 Cell Analyzer (BD Biosciences). BD FACSAria™ III Cell Sorter (BD Biosciences). Novocyte Quanteon (Agilent).

Software

BD FACSDiva™ Software, FlowJo v10

Cell population abundance

see manuscript

Gating strategy

see manuscript. extended figure 1

Tick this box to confirm that a figure exemplifying the gating strategy is provided in the Supplementary Information.